

Parquet solution for a flat Fermi surface

Anatoley T. Zheleznyak* and Victor M. Yakovenko†

Department of Physics and Center for Superconductivity Research, University of Maryland, College Park, MD 20742

Igor E. Dzyaloshinskii

Department of Physics, University of California, Irvine, CA 92717

(cond-mat/9609118, September 12, 1996)

We study instabilities occurring in the electron system whose Fermi surface has flat regions on its opposite sides. Such a Fermi surface resembles Fermi surfaces of some high- T_c superconductors. In the framework of the parquet approximation, we classify possible instabilities and derive renormalization-group equations that determine the evolution of corresponding susceptibilities with decreasing temperature. Numerical solutions of the parquet equations are found to be in qualitative agreement with a ladder approximation. For the repulsive Hubbard interaction, the antiferromagnetic (spin-density-wave) instability dominates, but when the Fermi surface is not perfectly flat, the d -wave superconducting instability takes over.

74.25.-q, 74.25.Dw, 74.72.-h, 75.30.Fv

I. INTRODUCTION

An interacting electron gas in one dimension has many unusual properties, such as the spin-charge separation, the power law of correlation functions, and the linear dependence of the electron relaxation rate on temperature and frequency (see Ref. [1] for a review). These one-dimensional (1D) results are well established, in many cases exactly, by applying a variety of mathematical methods including the Bethe Ansatz, the bosonization, and the parquet, or the renormalization group. To distinguish the exotic behavior of the 1D electron gas from a conventional Fermi-liquid behavior, Haldane introduced a concept of the so-called Luttinger liquid [2].

The discovery of high- T_c superconductivity renewed interest in the Luttinger-liquid concept. Anderson suggested that a two-dimensional (2D) electron gas behaves like the 1D Luttinger liquid, rather than a conventional Fermi liquid [3]. It is difficult to verify this claim rigorously, because the methods that prove the existence of the Luttinger liquid in 1D cannot be applied directly to higher dimensions. The Bethe Ansatz construction does not work in higher dimensions. The bosonization in higher dimensions [4–11] converts a system of interacting electrons into a set of harmonic oscillators representing the electron density modes. This procedure replaces the exact W_∞ commutation relations [6] with approximate boson commutators, which is a questionable, uncontrolled approximation. On the other hand, the parquet method, although not being as exact as the two other methods, has the advantage of being formulated as a certain selection rule within a standard many-body diagram technique; thus, it can be applied to higher dimensions rather straightforwardly. The parquet method has much in common with the renormalization-group treatment of Fermi liquids [12].

The 1D electron gas has two types of potential instabilities: the superconducting and the density-wave, which manifest themselves through logarithmic divergences of the corresponding one-loop susceptibilities with decreasing temperature. Within the parquet approach, a sum of an infinite series of diagrams, obtained by adding and inserting the two basic one-loop diagrams into each other, is calculated by solving a system of nonlinear differential equations, which are nothing but the renormalization-group equations [13]. This procedure was developed for the first time for meson scattering [14] and later was successfully applied to the 1D electron gas [15,16], as well as to the Kondo problem [17] and the X-ray absorption edge problem [18]. By considering both the superconducting and the density-wave instabilities on equal footing and adequately treating their competition, the parquet approximation differs from a conventional ladder (or mean-field) approximation, commonly applied in higher dimensions, where only one instability is taken into account. Under certain conditions in the 1D case, the superconducting and density-wave instabilities may cancel each other, giving rise to a non-trivial metallic ground state at zero temperature, namely the Luttinger liquid. In this case, the parquet derivation shows that the electron correlation functions have a power-law structure, which is one of the characteristic properties of the Luttinger liquid [16,19]. One may conclude that the competition between the superconducting and density-wave instabilities is an important ingredient of the Luttinger liquid theory.

In a generic higher-dimensional case, where density-wave instability does not exist or does not couple to superconducting instability because of corrugation of the Fermi surface, the parquet approach is not relevant. Nevertheless, there are a number of higher-dimensional models where the parquet is applicable and produces nontrivial results.

These include the models of multiple chains without single-electron hopping [20] and with single-electron hopping but in a magnetic field [21], as well as the model of an isotropic electron gas in a strong magnetic field [22,23]. In all of these models, the electron dispersion law is 1D, which permits to apply the parquet method; at the same time, the interaction between electrons is higher-dimensional, which makes a nontrivial difference from the purely 1D case. The particular version of the parquet method used in these cases is sometimes called the “fast” parquet, because, in addition to a “slow”, renormalization-group variable, the parquet equations acquire supplementary, “fast” variables, which label multiple electron states of the same energy.

Taking into account these considerations, it seems natural to start exploring a possibility of the Luttinger liquid behavior in higher dimensions by considering a model that combines 1D and higher-dimensional features. This is the model of an electron gas whose Fermi surface has flat regions on its opposite sides. The flatness means that within these regions the electron dispersion law is 1D: The electron energy depends only on the one component of momentum that is normal to the flat section. On the other hand, the size of the flat regions is finite, and that property differentiates the model from a purely 1D model, where the size is infinite, since nothing depends on the momenta perpendicular to the direction of a 1D chain. A particular case of the considered model is one where the 2D Fermi surface has a square shape. This model describes 2D electrons on a square lattice with the nearest-neighbor hopping at the half filling. It is a simplest model of the high- T_c superconductors.

The model has already attracted the attention of theorists. Virosztek and Ruvalds studied the “nested Fermi liquid” problem within a ladder or mean-field approximation [24,25]. Taking into account the 1D experience, this approach may be considered questionable, because it does not treat properly the competition between the superconducting and the density-wave channels. Houghton and Marston [7] mapped the flat parts of the Fermi surface onto discrete points. Such an oversimplification makes all scattering processes within the flat portion equivalent and artificially enhances the electron interaction. Mattis [26] and Hlubina [27] used the bosonization to treat the interaction between the electron density modes and claimed to solve the model exactly. However, mapping of the flat Fermi surface onto quantum chains and subsequent bosonization by Luther [28] indicated that the treatment of Mattis and Hlubina is insufficient, because the operators of backward and umklapp scattering on different quantum chains require a consistent renormalization-group treatment. Luther did not give solution to this problems, as well as he missed the interaction between the electrons located on four different quantum chains.

In the present paper, we solve the model consistently, using the fast parquet approach, where all possible instabilities occurring in the electron system with the flat regions on the Fermi surface are treated simultaneously. This approach was applied to the problem earlier [29] in order to explain the antiferromagnetism of chromium. In the present paper, we advance the study further by including the order parameters of the odd symmetry, missed in [29], performing detailed numerical calculations, and investigating the effect of a curvature of the Fermi surface. To simplify numerical calculations and to relate to the high- T_c superconductors, we consider the 2D case, although the method can be straightforwardly generalized to higher dimensions as well.

We find that the presence of the boundaries of the flat portions of the Fermi surface has a dramatic effect on the solutions of the parquet equations. Even if the initial vertex of interaction between electrons does not depend on the momenta along the Fermi surface (which are the “fast” variables), the vertex acquires a strong dependence on these variables upon renormalization, which greatly reduces the feedback coupling between the superconducting and density-wave channels relative to the 1D case. Instead of the two channels canceling each other, the leading channel, which is the spin-density-wave (SDW) in the case of the repulsive Hubbard interaction, develops its own phase transition, inducing on the way a considerable growth of the superconducting d -wave susceptibility. At the same time, the feedback from the superconducting to the SDW channel, very essential in the 1D case, is found negligible in the 2D case. These results are in qualitative agreement with the picture of the antiferromagnetically-induced d -wave superconductivity, which was developed within a ladder approximation for the flat Fermi surface in [25] and for a generic nested Hubbard model in [30]. Recent experiments strongly suggest that the high- T_c superconductivity is indeed of the d -wave type [31]. On the other hand, our results disagree with Refs. [26,27]. The origin of the discrepancy is that the bosonization arbitrarily replaces the exact W_∞ commutation relations [6] by approximate boson commutators; thus, the renormalization of the electron-electron interaction, which is an important part of the problem, becomes neglected.

In addition to having the flat sides, the square Fermi surface also has sharp corners, where the saddle points of the electron dispersion law, which produce the van Hove singularity in the density of states, are located. The presence of the van Hove singularity at the Fermi level enhances the divergence of the superconducting and density-wave loops to the square of the temperature logarithm. The fast parquet problem was formulated in this case in Ref. [32], where the contribution from the flat sides, being less divergent than the contribution from the saddle points, was neglected. The present paper completes the study by considering a Fermi surface with the flat sides and rounded corners, that is, without saddle points at the Fermi level. Our physical conclusions for both models are in qualitative agreement.

As photoemission experiments [33] demonstrate (see also [25]), many of the high- T_c superconductors indeed have flat regions on their Fermi surfaces. Hence, some of the results of this paper may be applicable to these materials.

However, the primary goal of our study is to elucidate general theoretical concepts rather than to achieve detailed description of real materials.

In order to distinguish the new features brought into the problems by introducing higher dimensions, we present material in an inductive manner. In Sec. II, we recall the derivation of the parquet equations in the simplest case of 1D spinless electrons. In Sec. III, we generalize the procedure to the case of 1D electrons with spin [15,16]. Then, we derive the parquet equations in the 2D case in Sec. IV and solve them numerically in Sec. V. The paper ends with conclusions in Sec. VI.

II. PARQUET EQUATIONS FOR ONE-DIMENSIONAL SPINLESS FERMIONS

Let us consider a 1D electron gas with a Fermi energy μ and a generic dispersion law $\varepsilon(k_x)$, where ε is the energy and k_x is the momentum of the electrons. As shown in Fig. 1, the Fermi surface of this system consists of two points located at $k_x = \pm k_F$, where k_F is the Fermi momentum. Assuming that the two points are well separated, let us treat the electrons whose momenta are close to $\pm k_F$ as two independent species and label them with the index \pm . In the vicinity of the Fermi energy, the dispersion laws of these electrons can be linearized:

$$\varepsilon_{\pm}(k_x) = \pm v_F k_x, \quad (2.1)$$

where the momenta k_x are counted from the respective Fermi points $\pm k_F$ for the two species of the electrons, $\pm v_F$ are the corresponding Fermi velocities, and the energy ε is counted from the chemical potential μ .

First, let us consider the simplest case of electrons without spin. The bare Hamiltonian of the interaction between the \pm electrons, \hat{H}_{int} , can be written as

$$\hat{H}_{\text{int}} = g \int \frac{dk_x^{(1)}}{2\pi} \frac{dk_x^{(2)}}{2\pi} \frac{dk_x^{(3)}}{2\pi} \hat{\psi}_+^{(1)}(k_x^{(1)} + k_x^{(2)} - k_x^{(3)}) \hat{\psi}_-^{(2)}(k_x^{(3)}) \hat{\psi}_+^{(1)}(k_x^{(1)}), \quad (2.2)$$

where g is the bare vertex of interaction, and the operators $\hat{\psi}_{\pm}^{\dagger}$ and $\hat{\psi}_{\pm}$ create and destroy the \pm electrons.

The tendencies toward the superconducting or density-wave ($2k_F$) instabilities in the system are reflected by the logarithmic divergences of the two one-loop diagrams shown in Fig. 2, where the solid and dashed lines represent the Green functions G_+ and G_- of the $+$ and $-$ electrons, respectively. The two diagrams in Fig. 2 differ in the mutual orientation of the arrows in the loops. In the Matsubara technique, the integration of the Green functions over the internal momentum k_x and energy ω_n produces the following expressions for the two diagrams:

$$\begin{aligned} & \pm T \sum_n \int \frac{dk_x}{2\pi} G_-(\mp\omega_n, \mp k_x) G_+(\omega_n + \Omega_n, k_x + q_x) \\ &= -T \sum_n \int \frac{dk_x}{2\pi} \frac{1}{(i\omega_n + v_F k_x)(i\omega_n + i\Omega_m - v_F(k_x + q_x))} \\ & \approx \frac{1}{2\pi v_F} \ln \left(\frac{\mu}{\max\{T, |v_F q_x|, |\Omega_m|\}} \right) \equiv \xi, \end{aligned} \quad (2.3)$$

where the upper sign corresponds to the superconducting and the lower to the density-wave susceptibility. In Eq. (2.3), T is the temperature, Ω_m is the external energy passing through the loop, and q_x is the external momentum for the superconducting loop and the deviation from $2k_F$ for the density-wave loop. With logarithmic accuracy, the value of the integral (2.3) is determined by the upper and lower cutoffs of the logarithmic divergence. In Eq. (2.3), the upper and lower cutoffs are written approximately, up to numerical coefficients of the order of unity, whose logarithms are small compared to $\xi \gg 1$. The variable ξ , introduced by Eq. (2.3), plays a very important role in the paper. Since ξ is the logarithm of the infrared cutoff, the increase of ξ represents renormalization toward low temperature and energy.

The two primary diagrams of Fig. 2 generate higher-order corrections to the vertex of interaction between electrons, γ , as illustrated in Fig. 3. In this Figure, the dots represent the bare interaction vertex g , whereas the renormalized vertex γ is shown as a circle. The one-loop diagrams in Fig. 3 are the same as in Fig. 2. The first two two-loop diagrams in Fig. 3 are obtained by repeating the same loop twice in a ladder manner. The last two diagrams are obtained by inserting one loop into the other and represent coupling between the two channels. The diagrams obtained by repeatedly adding and inserting the two basic diagrams of Fig. 2 in all possible ways are called the parquet diagrams. The ladder diagrams, where only the addition, but not the insertion of the loops is allowed, represent a subset of the more general set of the parquet diagrams. Selection of the parquet diagrams is justified, because, as one can check

calculating the diagrams in Fig. 3, they form a series with the expansion parameter $g\xi$: $\gamma = g \sum_{n=0}^{\infty} a_n(g\xi)^n$. If the bare interaction vertex g is small and the temperature is sufficiently low, so that $\xi(T)$ is big, one can argue [14–16] that nonparquet diagrams may be neglected, because their expansion parameter g is small compared to the parquet expansion parameter $g\xi$.

Every diagram in Fig. 3, except the bare vertex g , can be divided into two disconnected pieces by cutting one solid and one dashed line, the arrows of the cut lines being either parallel or antiparallel. The sum of those diagrams where the arrows of the cut lines are parallel (antiparallel) is called the superconducting (density-wave) “brick”. Thus, the vertex γ can be decomposed into the bare vertex g , the superconducting brick C , and the density-wave brick Z :

$$\gamma = g + C + Z. \quad (2.4)$$

Eq. (2.4) is illustrated in Fig. 4, where the bricks are represented as rectangles whose long sides, one being a solid and another a dashed line, represent the lines to be cut.

In a general case, the vertices and the bricks depend on the energies and momenta ($\omega_1, \omega_2, \omega_3, v_F k_x^{(1)}, v_F k_x^{(2)}$, and $v_F k_x^{(3)}$) of all incoming and outgoing electrons. Equations for the bricks can be found in closed form in the case where all their arguments are approximately equal within the logarithmic accuracy, that is, the ratios of the arguments and of their linear combinations are of the order of unity [14–16]. Practically, this means that all vertices and bricks are considered to be functions of the single renormalization-group variable ξ , defined in Eq. (2.3). It was proved in [14] that the two pieces obtained by cutting a brick are the full vertices of interaction, as illustrated graphically in Fig. 5. Analytically, the equations for the bricks are

$$C(\xi) = - \int_0^\xi d\zeta \gamma(\zeta) \gamma(\zeta), \quad (2.5a)$$

$$Z(\xi) = \int_0^\xi d\zeta \gamma(\zeta) \gamma(\zeta). \quad (2.5b)$$

The two vertices γ in the r.h.s. of Eqs. (2.5) represent the two pieces obtained from a brick by cutting, whereas the integrals over ζ represent the two connecting Green functions being integrated over the internal momentum and energy of the loop. The value of the renormalized vertex $\gamma(\zeta)$ changes as the integration over ζ progresses in Eqs. (2.5). In agreement with the standard rules of the diagram technique [34], a pair of the parallel (antiparallel) lines in Fig. 5 produces a negative (positive) sign in the r.h.s. of Eq. (2.5a) [(2.5b)].

Eqs. (2.5) can be rewritten in differential, renormalization-group form:

$$\frac{dC(\xi)}{d\xi} = -\gamma(\xi) \gamma(\xi), \quad C(\xi=0) = 0; \quad (2.6a)$$

$$\frac{dZ(\xi)}{d\xi} = \gamma(\xi) \gamma(\xi), \quad Z(\xi=0) = 0. \quad (2.6b)$$

Combining Eqs. (2.6) with Eq. (2.4), we find the renormalization equation for the full vertex γ :

$$\frac{d\gamma(\xi)}{d\xi} = \gamma(\xi) \gamma(\xi) - \gamma(\xi) \gamma(\xi) = 0, \quad (2.7a)$$

$$\gamma(\xi=0) = g. \quad (2.7b)$$

We see that the two terms in the r.h.s. of Eq. (2.7a), representing the tendencies toward density-wave and superconducting instabilities, exactly cancel each other. In a ladder approximation, where only one term is kept in the r.h.s., the result would be quite different, because $\gamma(\xi)$ would diverge at a finite ξ indicating an instability or generation of a pseudogap in the system.

In order to study possible instabilities in the system, we need to calculate corresponding generalized susceptibilities. For that purpose, let us add to the Hamiltonian of the system two fictitious infinitesimal external fields h_{SC} and h_{DW} that create the electron-electron and electron-hole pairs:

$$\begin{aligned} \hat{H}_{\text{ext}} = & \int \frac{dq_x}{2\pi} \frac{dk_x}{2\pi} \left[h_{\text{SC}}(q_x) \hat{\psi}_-^+ \left(\frac{q_x}{2} - k_x \right) \hat{\psi}_+^+ \left(\frac{q_x}{2} + k_x \right) \right. \\ & \left. + h_{\text{DW}}(q_x) \hat{\psi}_-^+ \left(k_x + \frac{q_x}{2} \right) \hat{\psi}_+^+ \left(k_x - \frac{q_x}{2} \right) + \text{H.c.} \right]. \end{aligned} \quad (2.8)$$

Now we need to introduce triangular vertices \mathcal{T}_{SC} and \mathcal{T}_{DW} that represent the response of the system to the fields h_{SC} and h_{DW} . Following the same procedure as in the derivation of the parquet equations for the bricks [15,16,22,29],

we find the parquet equations for the triangular vertices in graphic form, as shown in Fig. 6. In that Figure, the filled triangles represent the vertices \mathcal{T}_{SC} and \mathcal{T}_{DW} , whereas the dots represent the fields h_{SC} and h_{DW} . The circles, as in the other Figures, represent the interaction vertex γ . Analytically, these equations can be written as differential equations with given initial conditions:

$$\frac{d\mathcal{T}_{\text{SC}}(\xi)}{d\xi} = -\gamma(\xi)\mathcal{T}_{\text{SC}}(\xi), \quad \mathcal{T}_{\text{SC}}(0) = h_{\text{SC}}; \quad (2.9a)$$

$$\frac{d\mathcal{T}_{\text{DW}}(\xi)}{d\xi} = \gamma(\xi)\mathcal{T}_{\text{DW}}(\xi), \quad \mathcal{T}_{\text{DW}}(0) = h_{\text{DW}}. \quad (2.9b)$$

We will often refer to the triangular vertices \mathcal{T} as the “order parameters”. Indeed, they are the superconducting and density-wave order parameters induced in the system by the external fields h_{SC} and h_{DW} . If, for a finite h_i ($i = \text{SC}, \text{DW}$), a vertex $\mathcal{T}_i(\xi)$, which is proportional to h_i , diverges when $\xi \rightarrow \xi_c$, this indicates that a *spontaneous* order parameter appears in the system, that is, the order parameter may have a finite value even when the external field h_i is zero. The external fields are introduced here only as auxiliary tools and are equal to zero in real systems. We also note that the two terms in the r.h.s. of Eq. (2.8) are not Hermitian self-conjugate; thus, the fields h_i are the complex fields. Consequently, the order parameters $\mathcal{T}_i(\xi)$ are also complex, so, generally speaking, \mathcal{T} and \mathcal{T}^* do not coincide. According to Eqs. (2.7), $\gamma(\xi) = g$, so Eqs. (2.9) have the following solution:

$$\mathcal{T}_{\text{SC}}(\xi) = h_{\text{SC}} \exp(-g\xi), \quad (2.10a)$$

$$\mathcal{T}_{\text{DW}}(\xi) = h_{\text{DW}} \exp(g\xi). \quad (2.10b)$$

Now we can calculate the susceptibilities. The lowest order corrections to the free energy of the system due to the introduction of the fields h_{SC} and h_{DW} , F_{SC} and F_{DW} , obey the parquet equations shown graphically in Fig. 7 and analytically below:

$$F_{\text{SC}}(\xi) = \int_0^\xi d\zeta \mathcal{T}_{\text{SC}}(\zeta) \mathcal{T}_{\text{SC}}^*(\zeta), \quad (2.11a)$$

$$F_{\text{DW}}(\xi) = \int_0^\xi d\zeta \mathcal{T}_{\text{DW}}(\zeta) \mathcal{T}_{\text{DW}}^*(\zeta). \quad (2.11b)$$

Substituting expressions (2.10) into Eqs. (2.11) and dropping the squares of h_{SC} and h_{DW} , we find the susceptibilities:

$$\chi_{\text{SC}}(\xi) = -[\exp(-2g\xi) - 1]/2g, \quad (2.12a)$$

$$\chi_{\text{DW}}(\xi) = [\exp(2g\xi) - 1]/2g. \quad (2.12b)$$

According to Eqs. (2.12), when the interaction between electrons is repulsive (attractive), that is, g is positive (negative), the density-wave (superconducting) susceptibility increases as temperature decreases ($T \rightarrow 0$ and $\xi \rightarrow \infty$):

$$\chi_{\text{DW}(\text{SC})}(\xi) \propto \exp(\pm 2g\xi) = \left(\frac{\mu}{\max\{T, |v_F q_x|, |\Omega_m|\}} \right)^{\pm 2g}. \quad (2.13)$$

Susceptibilities (2.13) have power dependence on the temperature and energy, which is one of the characteristic properties of the Luttinger liquid. The susceptibilities are finite at finite temperatures and diverge only at zero temperature, in agreement with the general theorem [35] that phase transitions are impossible at finite temperatures in 1D systems. Mathematically, the absence of divergence at finite ξ is due to the cancellation of the two terms in the r.h.s. of Eq. (2.7a) and subsequent nonrenormalization of $\gamma(\xi)$. This nontrivial 1D result can be obtained only within the parquet, but not the ladder approximation.

III. PARQUET EQUATIONS FOR ONE-DIMENSIONAL FERMIONS WITH SPIN

Now let us consider 1D electrons with spin. In this case, there are three vertices of interaction, conventionally denoted as γ_1 , γ_2 , and γ_3 , which represent backward, forward, and umklapp scattering, respectively [15,16]. Umklapp scattering should be considered only when the change of the total momentum of the electrons in the interaction process, $4k_F$, is equal to the crystal lattice wave vector, which may or may not be the case in a particular model. In

this paper, we do not consider the vertex γ_4 , which describes the interaction between the electrons of the same type (+ or -), because this vertex does not have logarithmic corrections. The bare Hamiltonian of the interaction, \hat{H}_{int} , can be written as

$$\begin{aligned} \hat{H}_{\text{int}} = & \sum_{\sigma, \tau, \rho, \nu=\uparrow\downarrow} \int \frac{dk_x^{(1)}}{2\pi} \frac{dk_x^{(2)}}{2\pi} \frac{dk_x^{(3)}}{2\pi} \\ & \times \left\{ (-g_1 \delta_{\rho\tau} \delta_{\sigma\nu} + g_2 \delta_{\rho\nu} \delta_{\sigma\tau}) \hat{\psi}_{\nu+}^+(k_x^{(1)} + k_x^{(2)} - k_x^{(3)}) \hat{\psi}_{\tau-}^+(k_x^{(3)}) \hat{\psi}_{\sigma-}(k_x^{(2)}) \hat{\psi}_{\rho+}(k_x^{(1)}) \right. \\ & \left. + [g_3 \delta_{\rho\nu} \delta_{\sigma\tau} \hat{\psi}_{\nu-}^+(k_x^{(1)} + k_x^{(2)} - k_x^{(3)}) \hat{\psi}_{\tau-}^+(k_x^{(3)}) \hat{\psi}_{\sigma+}(k_x^{(2)}) \hat{\psi}_{\rho+}(k_x^{(1)}) + \text{H.c.}] \right\}, \end{aligned} \quad (3.1)$$

where the coefficients g_{1-3} denote the bare (unrenormalized) values of the interaction vertices γ_{1-3} . The operators $\hat{\psi}_{\sigma s}^+$ and $\hat{\psi}_{\sigma s}$ create and destroy electrons of the type $s = \pm$ and the spin $\sigma = \uparrow\downarrow$. The spin structure of the interaction Hamiltonian is dictated by conservation of spin. We picture the interaction vertices in Fig. 8, where the solid and dashed lines represent the + and - electrons. The thin solid lines inside the circles indicate how spin is conserved: The spins of the incoming and outgoing electrons connected by a thin line are the same. According to the structure of Hamiltonian (3.1), the umklapp vertex γ_3 describes the process where two + electrons come in and two - electrons come out, whereas the complex conjugate vertex γ_3^* describes the reversed process.

The three vertices of interaction contain six bricks, as shown schematically in Fig. 9:

$$\gamma_1 = g_1 + C_1 + Z_1, \quad (3.2a)$$

$$\gamma_2 = g_2 + C_2 + Z_2, \quad (3.2b)$$

$$\gamma_3 = g_3 + Z_I + Z_{II}, \quad (3.2c)$$

where C_1 and C_2 are the superconducting bricks, and Z_1 , Z_2 , Z_I , and Z_{II} are the density-wave bricks. In Fig. 9, the thin solid lines inside the bricks represent spin conservation. The umklapp vertex has two density-wave bricks Z_I and Z_{II} , which differ in their spin structure.

Parquet equations for the bricks are derived in the same manner as in Sec. II by adding appropriate spin structure dictated by spin conservation. It is convenient to derive the equations graphically by demanding that the thin spin lines are continuous, as shown in Fig. 10. Corresponding analytic equations can be written using the following rules. A pair of parallel (antiparallel) lines connecting two vertices in Fig. 10 produces the negative (positive) sign. A closed loop of the two connecting lines produces an additional factor -2 due to summation over the two spin orientations of the electrons.

$$\frac{dC_1(\xi)}{d\xi} = -2\gamma_1(\xi) \gamma_2(\xi), \quad (3.3a)$$

$$\frac{dC_2(\xi)}{d\xi} = -\gamma_1^2(\xi) - \gamma_2^2(\xi), \quad (3.3b)$$

$$\frac{dZ_1(\xi)}{d\xi} = 2\gamma_1(\xi) \gamma_2(\xi) - 2\gamma_1^2(\xi), \quad (3.3c)$$

$$\frac{dZ_2(\xi)}{d\xi} = \gamma_2^2(\xi) + \gamma_3(\xi) \gamma_3^*(\xi), \quad (3.3d)$$

$$\frac{dZ_I(\xi)}{d\xi} = 2\gamma_3(\xi) [\gamma_2(\xi) - \gamma_1(\xi)], \quad (3.3e)$$

$$\frac{dZ_{II}(\xi)}{d\xi} = 2\gamma_3(\xi) \gamma_2(\xi). \quad (3.3f)$$

Combining Eqs. (3.2) and (3.3), we obtain the well-known closed equations for renormalization of the vertices [16]:

$$\frac{d\gamma_1(\xi)}{d\xi} = -2\gamma_1^2(\xi), \quad (3.4a)$$

$$\frac{d\gamma_2(\xi)}{d\xi} = -\gamma_1^2(\xi) + \gamma_3(\xi) \gamma_3^*(\xi), \quad (3.4b)$$

$$\frac{d\gamma_3(\xi)}{d\xi} = 2\gamma_3(\xi) [2\gamma_2(\xi) - \gamma_1(\xi)]. \quad (3.4c)$$

In the presence of spin, the electron operators in Eq. (2.8) and, correspondingly, the fields h_i and the triangular vertices $\mathcal{T}_i(\xi)$ acquire the spin indices. Thus, the superconducting triangular vertex $\mathcal{T}_{\text{SC}}(\xi)$ becomes a vector:

$$\mathcal{T}_{\text{SC}}(\xi) = \begin{pmatrix} \mathcal{T}_{\text{SC}}^{\uparrow\uparrow}(\xi) \\ \mathcal{T}_{\text{SC}}^{\uparrow\downarrow}(\xi) \\ \mathcal{T}_{\text{SC}}^{\downarrow\uparrow}(\xi) \\ \mathcal{T}_{\text{SC}}^{\downarrow\downarrow}(\xi) \end{pmatrix}. \quad (3.5)$$

Parquet equations for the triangular vertices are given by the diagrams shown in Fig. 6, where the spin lines should be added in the same manner as in Fig. 10. The superconducting vertex obeys the following equation:

$$\frac{d\mathcal{T}_{\text{SC}}(\xi)}{d\xi} = \Gamma_{\text{SC}}(\xi) \mathcal{T}_{\text{SC}}(\xi), \quad (3.6)$$

where the matrix $\Gamma_{\text{SC}}(\xi)$ is

$$\Gamma_{\text{SC}}(\xi) = \begin{pmatrix} -\gamma_2 + \gamma_1 & 0 & 0 & 0 \\ 0 & -\gamma_2 & \gamma_1 & 0 \\ 0 & \gamma_1 & -\gamma_2 & 0 \\ 0 & 0 & 0 & -\gamma_2 + \gamma_1 \end{pmatrix}. \quad (3.7)$$

Linear equation (3.6) is diagonalized by introducing the singlet, \mathcal{T}_{SSC} , and the triplet, \mathcal{T}_{TSC} , superconducting triangular vertices:

$$\mathcal{T}_{\text{SSC}}(\xi) = \mathcal{T}_{\text{SC}}^{\uparrow\downarrow}(\xi) - \mathcal{T}_{\text{SC}}^{\downarrow\uparrow}(\xi), \quad (3.8a)$$

$$\mathcal{T}_{\text{TSC}}(\xi) = \begin{pmatrix} \mathcal{T}_{\text{SC}}^{\uparrow\uparrow}(\xi) \\ \mathcal{T}_{\text{SC}}^{\uparrow\downarrow}(\xi) + \mathcal{T}_{\text{SC}}^{\downarrow\uparrow}(\xi) \\ \mathcal{T}_{\text{SC}}^{\downarrow\downarrow}(\xi) \end{pmatrix}, \quad (3.8b)$$

which obey the following equations:

$$\frac{d\mathcal{T}_{\text{SSC}(\text{TSC})}(\xi)}{d\xi} = [\mp\gamma_1(\xi) - \gamma_2(\xi)] \mathcal{T}_{\text{SSC}(\text{TSC})}(\xi). \quad (3.9)$$

In Eq. (3.9) the sign $-$ and the index SSC correspond to the singlet superconductivity, whereas the sign $+$ and the index TSC correspond to the triplet one. In the rest of the paper, we use the index SC where discussion applies to both SSC and TSC .

Now let us consider the density-wave triangular vertices, first in the absence of umklapp. They form a vector

$$\mathcal{T}_{\text{DW}}(\xi) = \begin{pmatrix} \mathcal{T}_{\text{DW}}^{\uparrow\uparrow}(\xi) \\ \mathcal{T}_{\text{DW}}^{\uparrow\downarrow}(\xi) \\ \mathcal{T}_{\text{DW}}^{\downarrow\uparrow}(\xi) \\ \mathcal{T}_{\text{DW}}^{\downarrow\downarrow}(\xi) \end{pmatrix}, \quad (3.10)$$

which obeys the equation

$$\frac{d\mathcal{T}_{\text{DW}}(\xi)}{d\xi} = \Gamma_{\text{DW}}(\xi) \mathcal{T}_{\text{DW}}(\xi) \quad (3.11)$$

with the matrix

$$\Gamma_{\text{DW}}(\xi) = \begin{pmatrix} -\gamma_1 + \gamma_2 & 0 & 0 & -\gamma_1 \\ 0 & \gamma_2 & 0 & 0 \\ 0 & 0 & \gamma_2 & 0 \\ -\gamma_1 & 0 & 0 & -\gamma_1 + \gamma_2 \end{pmatrix}. \quad (3.12)$$

Eq. (3.11) is diagonalized by introducing the charge-, \mathcal{T}_{CDW} , and the spin-, \mathcal{T}_{SDW} , density-wave triangular vertices:

$$\mathcal{T}_{\text{CDW}}(\xi) = \mathcal{T}_{\text{DW}}^{\uparrow\uparrow}(\xi) + \mathcal{T}_{\text{DW}}^{\downarrow\downarrow}(\xi), \quad (3.13a)$$

$$\mathcal{T}_{\text{SDW}}(\xi) = \begin{pmatrix} \mathcal{T}_{\text{DW}}^{\uparrow\downarrow}(\xi) \\ \mathcal{T}_{\text{DW}}^{\downarrow\uparrow}(\xi) \\ \mathcal{T}_{\text{DW}}^{\uparrow\uparrow}(\xi) - \mathcal{T}_{\text{DW}}^{\downarrow\downarrow}(\xi) \end{pmatrix}, \quad (3.13b)$$

which obey the following equations:

$$\frac{d\mathcal{T}_{\text{CDW}}(\xi)}{d\xi} = [-2\gamma_1(\xi) + \gamma_2(\xi)] \mathcal{T}_{\text{CDW}}(\xi), \quad (3.14a)$$

$$\frac{d\mathcal{T}_{\text{SDW}}(\xi)}{d\xi} = \gamma_2(\xi) \mathcal{T}_{\text{SDW}}(\xi). \quad (3.14b)$$

When the umklapp vertices γ_3 and γ_3^* are introduced, they become offdiagonal matrix elements in Eqs. (3.14), mixing \mathcal{T}_{CDW} and \mathcal{T}_{SDW} with their complex conjugates. Assuming for simplicity that γ_3 is real, we find that the following linear combinations diagonalize the equations:

$$\mathcal{T}_{\text{CDW(SDW)}\pm} = \mathcal{T}_{\text{CDW(SDW)}} \pm \mathcal{T}_{\text{CDW(SDW)}}^*, \quad (3.15)$$

and the equations become:

$$\frac{d\mathcal{T}_{\text{CDW}\pm}(\xi)}{d\xi} = [-2\gamma_1(\xi) + \gamma_2(\xi) \mp \gamma_3(\xi)] \mathcal{T}_{\text{CDW}\pm}(\xi), \quad (3.16a)$$

$$\frac{d\mathcal{T}_{\text{SDW}\pm}(\xi)}{d\xi} = [\gamma_2(\xi) \pm \gamma_3(\xi)] \mathcal{T}_{\text{SDW}\pm}(\xi). \quad (3.16b)$$

If the external fields h_i are set to unity in the initial conditions of the type (2.9) for all triangular vertices $i = \text{SSC, TSC, CDW}\pm, \text{SDW}\pm$, then the corresponding susceptibilities are equal numerically to the free energy corrections of the type (2.11):

$$\chi_i(\xi) = \int_0^\xi d\zeta \mathcal{T}_i(\zeta) \mathcal{T}_i^*(\zeta). \quad (3.17)$$

Eqs. (3.4), (3.9), (3.16), and (3.17) were solved analytically in Ref. [16], where a complete phase diagram of the 1D electron gas with spin was obtained.

IV. PARQUET EQUATIONS FOR TWO-DIMENSIONAL ELECTRONS

Now let us consider a 2D electron gas with the Fermi surface shown schematically in Fig. 11. It contains two pairs of flat regions, shown as the thick lines and labeled by the letters a and b . Such a Fermi surface resembles the Fermi surfaces of some high- T_c superconductors [33]. In our consideration, we restrict the momenta of electrons to the flat sections only. In this way, we effectively neglect the rounded portions of the Fermi surface, which are not relevant for the parquet consideration, because the density-wave loop is not divergent there. One can check also that the contributions of the portions a and b do not mix with each other in the parquet manner, so they may be treated separately. For this reason, we will consider only the region a , where the 2D electron states are labeled by the two momenta k_x and k_y , the latter momentum being restricted to the interval $[-k_y^{(0)}, k_y^{(0)}]$. In our model, the energy of electrons depends only on the momentum k_x according to Eq. (2.1) and does not depend on the momentum k_y . We neglect possible dependence of the Fermi velocity v_F on k_y ; it was argued in Ref. [28] that this dependence is irrelevant in the renormalization-group sense.

In the 2D case, each brick or vertex of interaction between electrons acquires extra variables $k_y^{(1)}$, $k_y^{(2)}$, and $k_y^{(3)}$ in addition to the 1D variables ω_1 , ω_2 , ω_3 , $v_F k_x^{(1)}$, $v_F k_x^{(2)}$, and $v_F k_x^{(3)}$. These two sets of variables play very different roles. The Green functions, which connect the vertices and produce the logarithms ξ , depend only on the second set of variables. Thus, following the parquet approach outlined in the previous Sections, we dump all the ω and $v_F k_x$ variables of a vertex or a brick into a single variable ξ . At the same time, the $k_y^{(1)}$, $k_y^{(2)}$, and $k_y^{(3)}$ variables remain independent and play the role of indices labeling the vertices, somewhat similar to the spin indices. Thus, each vertex and brick is a function of several variables, which we will always write in the following order: $\gamma(k_y^{(1)}, k_y^{(2)}; k_y^{(3)}, k_y^{(4)}; \xi)$.

It is implied that the first four variables satisfy the momentum conservation law $k_y^{(1)} + k_y^{(2)} = k_y^{(3)} + k_y^{(4)}$, and each of them belongs to the interval $[-k_y^{(0)}, k_y^{(0)}]$. The assignment of the variables $k_y^{(1)}$, $k_y^{(2)}$, $k_y^{(3)}$, and $k_y^{(4)}$ to the ends of the vertices and bricks is shown in Fig. 9, where the labels k_j ($j = 1 - 4$) should be considered now as the variables $k_y^{(j)}$. To shorten notation, it is convenient to combine these variable into a single four-component vector

$$\mathcal{K} = (k_y^{(1)}, k_y^{(2)}; k_y^{(3)}, k_y^{(4)}), \quad (4.1)$$

so that the relation between the vertices and the bricks can be written as

$$\gamma_1(\mathcal{K}, \xi) = g_1 + C_1(\mathcal{K}, \xi) + Z_1(\mathcal{K}, \xi), \quad (4.2a)$$

$$\gamma_2(\mathcal{K}, \xi) = g_2 + C_2(\mathcal{K}, \xi) + Z_2(\mathcal{K}, \xi), \quad (4.2b)$$

$$\gamma_3(\mathcal{K}, \xi) = g_3 + Z_I(\mathcal{K}, \xi) + Z_{II}(\mathcal{K}, \xi). \quad (4.2c)$$

After this introduction, we are in a position to write the parquet equations for the bricks. These equations are shown graphically in Fig. 10, where again the momenta k_j should be understood as $k_y^{(j)}$. Analytically, the equations are written below, with the terms in the same order as in Fig. 10:

$$\frac{\partial C_1(\mathcal{K}, \xi)}{\partial \xi} = -\gamma_1(\mathcal{K}_1, \xi) \circ \gamma_2(\mathcal{K}'_1, \xi) - \gamma_2(\mathcal{K}_1, \xi) \circ \gamma_1(\mathcal{K}'_1, \xi), \quad (4.3a)$$

$$\frac{\partial C_2(\mathcal{K}, \xi)}{\partial \xi} = -\gamma_1(\mathcal{K}_1, \xi) \circ \gamma_1(\mathcal{K}'_1, \xi) - \gamma_2(\mathcal{K}_1, \xi) \circ \gamma_2(\mathcal{K}'_1, \xi), \quad (4.3b)$$

$$\begin{aligned} \frac{\partial Z_1(\mathcal{K}, \xi)}{\partial \xi} = & \gamma_1(\mathcal{K}_2, \xi) \circ \gamma_2(\mathcal{K}'_2, \xi) + \gamma_2(\mathcal{K}_2, \xi) \circ \gamma_1(\mathcal{K}'_2, \xi) - 2\gamma_1(\mathcal{K}_2, \xi) \circ \gamma_1(\mathcal{K}'_2, \xi) \\ & - 2\tilde{\gamma}_3(\mathcal{K}_2, \xi) \circ \tilde{\gamma}_3(\mathcal{K}'_2, \xi) + \tilde{\gamma}_3(\mathcal{K}_2, \xi) \circ \tilde{\gamma}_3(\mathcal{K}'_2, \xi) + \gamma_3(\mathcal{K}_2, \xi) \circ \tilde{\gamma}_3(\mathcal{K}'_2, \xi), \end{aligned} \quad (4.3c)$$

$$\frac{\partial Z_2(\mathcal{K}, \xi)}{\partial \xi} = \gamma_2(\mathcal{K}_2, \xi) \circ \gamma_2(\mathcal{K}'_2, \xi) + \gamma_3(\mathcal{K}_2, \xi) \circ \tilde{\gamma}_3(\mathcal{K}'_2, \xi), \quad (4.3d)$$

$$\begin{aligned} \frac{\partial Z_I(\mathcal{K}, \xi)}{\partial \xi} = & \tilde{\gamma}_3(\mathcal{K}_3, \xi) \circ \gamma_2(\mathcal{K}'_3, \xi) + \gamma_2(\mathcal{K}_3, \xi) \circ \tilde{\gamma}_3(\mathcal{K}'_3, \xi) + \gamma_1(\mathcal{K}_3, \xi) \circ \gamma_3(\mathcal{K}'_3, \xi) \\ & + \gamma_3(\mathcal{K}_3, \xi) \circ \gamma_1(\mathcal{K}'_3, \xi) - 2\tilde{\gamma}_3(\mathcal{K}_3, \xi) \circ \gamma_1(\mathcal{K}'_3, \xi) - 2\gamma_1(\mathcal{K}_3, \xi) \circ \tilde{\gamma}_3(\mathcal{K}'_3, \xi), \end{aligned} \quad (4.3e)$$

$$\frac{\partial Z_{II}(\mathcal{K}, \xi)}{\partial \xi} = \gamma_3(\mathcal{K}_2, \xi) \circ \gamma_2(\mathcal{K}''_2, \xi) + \gamma_2(\mathcal{K}_2, \xi) \circ \gamma_3(\mathcal{K}''_2, \xi), \quad (4.3f)$$

where

$$\mathcal{K}_1 = (k_y^{(1)}, k_y^{(2)}; k_y^{(A)}, k_y^{(B)}), \quad \mathcal{K}'_1 = (k_y^{(B)}, k_y^{(A)}; k_y^{(3)}, k_y^{(4)}), \quad (4.4a)$$

$$\mathcal{K}_2 = (k_y^{(1)}, k_y^{(B)}; k_y^{(3)}, k_y^{(A)}), \quad \mathcal{K}'_2 = (k_y^{(A)}, k_y^{(2)}; k_y^{(B)}, k_y^{(4)}), \quad \mathcal{K}''_2 = (k_y^{(2)}, k_y^{(A)}; k_y^{(4)}, k_y^{(B)}), \quad (4.4b)$$

$$\mathcal{K}_3 = (k_y^{(1)}, k_y^{(B)}; k_y^{(4)}, k_y^{(A)}), \quad \mathcal{K}'_3 = (k_y^{(2)}, k_y^{(A)}; k_y^{(3)}, k_y^{(B)}), \quad (4.4c)$$

and the tilde and the bar operations are defined as

$$\tilde{\gamma}_j(k_y^{(1)}, k_y^{(2)}; k_y^{(3)}, k_y^{(4)}; \xi) \equiv \gamma_j(k_y^{(1)}, k_y^{(2)}; k_y^{(4)}, k_y^{(3)}; \xi), \quad (4.5a)$$

$$\bar{\gamma}_3(k_y^{(1)}, k_y^{(2)}; k_y^{(3)}, k_y^{(4)}; \xi) \equiv \gamma_3^*(k_y^{(4)}, k_y^{(3)}; k_y^{(2)}, k_y^{(1)}; \xi). \quad (4.5b)$$

In Eqs. (4.3), we introduced the operation \circ that represents the integration over the internal momenta of the loops in Fig. 10. It denotes the integration over the intermediate momentum $k_y^{(A)}$ with the restriction that both $k_y^{(A)}$ and $k_y^{(B)}$, another intermediate momentum determined by conservation of momentum, belong to the interval $[-k_y^{(0)}, k_y^{(0)}]$. For example, the explicit form of the first term in the r.h.s. of Eq. (4.3a) is:

$$\begin{aligned} \gamma_1(\mathcal{K}_1, \xi) \circ \gamma_2(\mathcal{K}'_1, \xi) = & \int_{-k_y^{(0)} \leq k_y^{(A)} \leq k_y^{(0)}; -k_y^{(0)} \leq k_y^{(1)} + k_y^{(2)} - k_y^{(A)} \leq k_y^{(0)}} \frac{dk_y^{(A)}}{2\pi} \\ & \times \gamma_1(k_y^{(1)}, k_y^{(2)}; k_y^{(A)}, k_y^{(1)} + k_y^{(2)} - k_y^{(A)}; \xi) \gamma_2(k_y^{(1)} + k_y^{(2)} - k_y^{(A)}, k_y^{(A)}; k_y^{(3)}, k_y^{(4)}; \xi). \end{aligned} \quad (4.6)$$

Eqs. (4.3) and (4.2) with definitions (4.1), (4.4), and (4.5) form a closed system of integrodifferential equations, which will be solved numerically in Sec. V. The initial conditions for Eqs. (4.3) and (4.2) are that all the C and Z bricks are equal to zero at $\xi = 0$.

Parquet equations for the superconducting triangular vertices can be found in the 2D case by adding the k_y momenta to the 1D equations (3.9). The equations are shown graphically in Fig. 6, where the momenta k and q should be interpreted as k_y and q_y :

$$\frac{\partial \mathcal{T}_{\text{SSC}(\text{TSC})}(k_y, q_y, \xi)}{\partial \xi} = f_{\text{SSC}(\text{TSC})}(\mathcal{K}_{\text{SC}}, \xi) \circ \mathcal{T}_{\text{SSC}(\text{TSC})}(k'_y, q_y, \xi), \quad (4.7)$$

where

$$f_{\text{SSC}(\text{TSC})}(\mathcal{K}_{\text{SC}}, \xi) = \mp \gamma_1(\mathcal{K}_{\text{SC}}, \xi) - \gamma_2(\mathcal{K}_{\text{SC}}, \xi), \quad (4.8)$$

$$\mathcal{K}_{\text{SC}} = (k'_y + q_y/2, -k'_y + q_y/2; -k_y + q_y/2, k_y + q_y/2), \quad (4.9)$$

and the operator \circ denotes the integration over k'_y with the restriction that both $k'_y + q_y/2$ and $-k'_y + q_y/2$ belong to the interval $[-k_y^{(0)}, k_y^{(0)}]$. The \mp signs in front of γ_1 in Eq. (4.8) correspond to the singlet and triplet superconductivity. As discussed in Sec. II, the triangular vertex $\mathcal{T}_{\text{SC}}(k_y, q_y, \xi)$ is the superconducting order parameter, q_y and k_y being the y -components of the total and the relative momenta of the electrons in a Cooper pair. Indeed, the vertex $\mathcal{T}_{\text{SC}}(k_y, q_y, \xi)$ obeys the linear equation shown in Fig. 6, which is the linearized Gorkov equation for the superconducting order parameter. As the system approaches a phase transition, the vertex $\mathcal{T}_{\text{SC}}(k_y, q_y, \xi)$ diverges in overall magnitude, but its dependence on k_y for a fixed q_y remains the same, up to a singular, ξ -dependent factor. The dependence of $\mathcal{T}_{\text{SC}}(k_y, q_y, \xi)$ on k_y describes the distribution of the emerging order parameter over the Fermi surface. The numerically found behavior of $\mathcal{T}_{\text{SC}}(k_y, q_y, \xi)$ is discussed in Sec. V.

Due to the particular shape of the Fermi surface, the vertices of interaction in our 2D model have two special symmetries: with respect to the sign change of all momenta k_y and with respect to the exchange of the + and - electrons:

$$\gamma_i(k_y^{(1)}, k_y^{(2)}; k_y^{(3)}, k_y^{(4)}; \xi) = \gamma_i(-k_y^{(1)}, -k_y^{(2)}; -k_y^{(3)}, -k_y^{(4)}; \xi), \quad i = 1, 2, 3; \quad (4.10a)$$

$$\gamma_i(k_y^{(1)}, k_y^{(2)}; k_y^{(3)}, k_y^{(4)}; \xi) = \gamma_i(k_y^{(2)}, k_y^{(1)}; k_y^{(4)}, k_y^{(3)}; \xi), \quad i = 1, 2, 3; \quad (4.10b)$$

$$\gamma_3(k_y^{(1)}, k_y^{(2)}; k_y^{(3)}, k_y^{(4)}; \xi) = \gamma_3(k_y^{(4)}, k_y^{(3)}; k_y^{(2)}, k_y^{(1)}; \xi), \quad (4.10c)$$

where in Eq. (4.10c) we assume for simplicity that γ_3 is real. As a consequence of (4.10), Eqs. (4.7) are invariant with respect to the sign reversal of k_y in $\mathcal{T}_{\text{SC}}(k_y, q_y, \xi)$ at a fixed q_y . The following combinations of the triangular vertices form two irreducible representations of this symmetry, that is, they are independent and do not mix in Eqs. (4.7):

$$\mathcal{T}_{\text{SSC}(\text{TSC})}^{\pm}(k_y, q_y, \xi) = \mathcal{T}_{\text{SSC}(\text{TSC})}(k_y, q_y, \xi) \pm \mathcal{T}_{\text{SSC}(\text{TSC})}(-k_y, q_y, \xi). \quad (4.11)$$

The triangular vertices $\mathcal{T}_{\text{SSC}(\text{TSC})}^{\pm}(k_y, q_y, \xi)$ describe the superconducting order parameters that are either symmetric or antisymmetric with respect to the sign change of k_y . When $\mathcal{T}_{\text{SSC}}^+$ is extended over the whole 2D Fermi surface (see Fig. 11), it acquires the s -wave symmetry, whereas $\mathcal{T}_{\text{SSC}}^-$ the d -wave symmetry. The symmetrized vertices $\mathcal{T}_{\text{SSC}(\text{TSC})}^{\pm}(k_y, q_y, \xi)$ obey the same Eqs. (4.7) as the unsymmetrized ones.

The equations for the density-wave triangular vertices are obtained in a similar manner:

$$\frac{\partial \mathcal{T}_{\text{CDW}\pm}^{\pm}(k_y, q_y, \xi)}{\partial \xi} = f_{\text{CDW}\pm}(\mathcal{K}_{\text{DW}}, \xi) \circ \mathcal{T}_{\text{CDW}\pm}^{\pm}(k'_y, q_y, \xi), \quad (4.12a)$$

$$\frac{\partial \mathcal{T}_{\text{SDW}\pm}^{\pm}(k_y, q_y, \xi)}{\partial \xi} = f_{\text{SDW}\pm}(\mathcal{K}_{\text{DW}}, \xi) \circ \mathcal{T}_{\text{SDW}\pm}^{\pm}(k'_y, q_y, \xi), \quad (4.12b)$$

where

$$f_{\text{CDW}\pm}(\mathcal{K}_{\text{DW}}, \xi) = -2\gamma_1(\mathcal{K}_{\text{DW}}, \xi) \mp 2\gamma_3(\mathcal{K}_{\text{DW}}, \xi) + \gamma_2(\mathcal{K}_{\text{DW}}, \xi) \pm \gamma_3(\mathcal{K}_{\text{DW}}, \xi), \quad (4.13)$$

$$f_{\text{SDW}\pm}(\mathcal{K}_{\text{DW}}, \xi) = \gamma_2(\mathcal{K}_{\text{DW}}, \xi) \pm \gamma_3(\mathcal{K}_{\text{DW}}, \xi), \quad (4.14)$$

$$\mathcal{K}_{\text{DW}} = (k'_y + q_y/2, k_y - q_y/2; k'_y - q_y/2, k_y + q_y/2). \quad (4.15)$$

The \pm signs in the subscripts of \mathcal{T} in Eqs. (4.12) and in front of γ_3 in Eqs. (4.13)–(4.14) refer to the umklapp symmetry discussed in Sec. III, whereas the \pm signs in the superscripts of \mathcal{T} refer to the symmetry with respect to sign reversal of k_y , discussed above in the superconducting case. The k_y -antisymmetric density waves are actually the waves of charge current and spin current [36,32], also known in the so-called flux phases [37].

Once the triangular vertices \mathcal{T}_i are found, the corresponding susceptibilities χ_i are calculated according to the following equation, similar to Eq. (3.17):

$$\chi_i(q_y, \xi) = \int_0^\xi d\zeta \int \frac{dk_y}{2\pi} \mathcal{T}_i(k_y, q_y, \zeta) \mathcal{T}_i^*(k_y, q_y, \zeta), \quad (4.16)$$

where the integration over k_y is restricted so that both $k_y \pm q_y/2$ belong to the interval $[-k_y^{(0)}, k_y^{(0)}]$.

Using functions (4.8), (4.13), and (4.14) and symmetries (4.10), we can rewrite Eqs. (4.3) in a more compact form. For that purpose, we introduce the SSC, TSC, CDW, and SDW bricks that are the linear combinations of the original bricks:

$$C_{\text{SSC}(\text{TSC})} = C_2 \pm C_1, \quad (4.17a)$$

$$Z_{\text{CDW}\pm} = \tilde{Z}_2 - 2\tilde{Z}_1 \pm (\tilde{Z}_{II} - 2Z_I), \quad (4.17b)$$

$$Z_{\text{SDW}\pm} = Z_2 \pm Z_{II}, \quad (4.17c)$$

where the tilde operation is defined in Eq. (4.5a). Then, Eqs. (4.3) become:

$$\frac{\partial C_{\text{SSC}(\text{TSC})}(\mathcal{K}, \xi)}{\partial \xi} = -f_{\text{SSC}(\text{TSC})}(\mathcal{K}_1, \xi) \circ f_{\text{SSC}(\text{TSC})}(\mathcal{K}'_1, \xi), \quad (4.18a)$$

$$\frac{\partial Z_{\text{CDW}\pm}(\mathcal{K}, \xi)}{\partial \xi} = f_{\text{CDW}\pm}(\mathcal{K}_3, \xi) \circ f_{\text{CDW}\pm}(\mathcal{K}'_3, \xi), \quad (4.18b)$$

$$\frac{\partial Z_{\text{SDW}\pm}(\mathcal{K}, \xi)}{\partial \xi} = f_{\text{SDW}\pm}(\mathcal{K}_2, \xi) \circ f_{\text{SDW}\pm}(\mathcal{K}'_2, \xi). \quad (4.18c)$$

The parquet equations in the form (4.18) were obtained in Ref. [29].

It is instructive to trace the difference between the parquet equations (4.18) and the corresponding ladder equations. Suppose that, for some reason, only one brick, say C_{SSC} , among the six bricks (4.17) is appreciable, whereas the other bricks may be neglected. Using definitions (4.2) and (4.8), we find that Eq. (4.18a) becomes a closed equation:

$$\frac{\partial f_{\text{SSC}}(\mathcal{K}, \xi)}{\partial \xi} = f_{\text{SSC}}(\mathcal{K}_1, \xi) \circ f_{\text{SSC}}(\mathcal{K}'_1, \xi), \quad (4.19)$$

where

$$f_{\text{SSC}}(\mathcal{K}_1, \xi) = -g_1 - g_2 - C_{\text{SSC}}(\mathcal{K}, \xi). \quad (4.20)$$

Eq. (4.19) is the ladder equation for the singlet superconductivity. When the initial value $-(g_1 + g_2)$ of the vertex f_{SSC} is positive, Eq. (4.19) has a singular solution ($f_{\text{SSC}} \rightarrow \infty$ at $\xi \rightarrow \xi_c$), which describes a phase transition into the singlet superconducting state at a finite temperature. Repeating this consideration for every channel, we construct the phase diagram of the system in the ladder approximation as a list of necessary conditions for the corresponding instabilities:

$$\text{SSC} : \quad g_1 + g_2 < 0, \quad (4.21a)$$

$$\text{TSC} : \quad -g_1 + g_2 < 0, \quad (4.21b)$$

$$\text{CDW+} : \quad -2g_1 + g_2 - g_3 > 0, \quad (4.21c)$$

$$\text{CDW-} : \quad -2g_1 + g_2 + g_3 > 0, \quad (4.21d)$$

$$\text{SDW+} : \quad g_2 + g_3 > 0, \quad (4.21e)$$

$$\text{SDW-} : \quad g_2 - g_3 > 0. \quad (4.21f)$$

The difference between the ladder and the parquet approximations shows up when there are more than one appreciable bricks in the problem. Then, the vertex f_{SSC} contains not only the brick C_{SSC} , but other bricks as well, so Eqs. (4.18) get coupled. This is the case, for example, for the 1D spinless electrons, where the bricks C and Z are equally big, so they cancel each other in γ (see Sec. II).

V. RESULTS OF NUMERICAL CALCULATIONS

The numerical procedure consists of three consecutive steps; each of them involves solving differential equations by the fourth-order Runge–Kutta method. First, we solve parquet equations (4.2) and (4.3) for the interaction vertices, which are closed equations. Then, we find the triangular vertices \mathcal{T}_i , whose equations (4.7) and (4.12) involve the interaction vertices γ_i through Eqs. (4.8), (4.13), and (4.14). Finally, we calculate the susceptibilities χ_i from Eqs. (4.16), which depend on the triangular vertices \mathcal{T}_i .

We select the initial conditions for the interaction vertices to be independent of the transverse momenta \mathcal{K} : $\gamma_i(\mathcal{K}, \xi=0) = g_i$. The momentum-independent interaction naturally appears in the Hubbard model, where the interaction is local in real space. In this Chapter, the results are shown mostly for the repulsive Hubbard model without umklapp: $g_1 = g_2 = g$, $g_3 = 0$ (Figs. 12–17), or with umklapp: $g_1 = g_2 = g_3 = g$ (Figs. 18–19), where g is proportional the Hubbard interaction constant U . The absolute value of g (but not the sign of g) is not essential in our calculations, because it can be removed from the equations by redefining ξ to $\xi' = |g|\xi$. After the redefinition, we effectively have $|g| = 1$ in the initial conditions. The actual value of $|g|$ matters only when the logarithmic variable ξ' is converted into the temperature according to the formula $T = \mu \exp(-2\pi v_F \xi'/|g|)$.

The initial independence of $\gamma_i(\mathcal{K}, \xi=0)$ on \mathcal{K} does not imply that this property is preserved upon renormalization. On the contrary, during renormalization, $\gamma_i(\mathcal{K}, \xi)$ develops a very strong dependence on \mathcal{K} and may even change sign in certain regions of the \mathcal{K} -space. We illustrate this statement in Fig. 12 by showing typical dependences of $\gamma_1(\mathcal{K}, \xi)$ and $\gamma_2(\mathcal{K}, \xi)$ on the average momentum $p_y = (k_y^{(1)} + k_y^{(2)})/2$ of the incoming electrons at $k_1 = k_3$ and $k_2 = k_4$ after some renormalization ($\xi = 1.4$). In Figs. 12–14, the upper and lower limits on the horizontal axes are the boundaries $\pm k_y^{(0)}$ of the flat region on the Fermi surface, which are set to ± 1 without loss of generality. One can observe in Fig. 12 that the electron-electron interaction becomes negative (attractive) at large p_y , even though initially it was repulsive everywhere.

Mathematically, the dependence of $\gamma_i(\mathcal{K}, \xi)$ on \mathcal{K} arises because of the finite limits of integration, $[-k_y^{(0)}, k_y^{(0)}]$, imposed on the variables $k_y^{(A)}$ and $k_y^{(B)}$ in Eqs. (4.3). For example, in Eq. (4.3a), when $p_y = (k_y^{(1)} + k_y^{(2)})/2$ equals zero, $k_y^{(A)}$ may change from $-k_y^{(0)}$ to $k_y^{(0)}$ while $k_y^{(B)}$ stays in the same interval. However, when $p_y > 0$, $k_y^{(A)}$ has to be confined to a narrower interval $[-k_y^{(0)} + 2p_y, k_y^{(0)}]$ to ensure that $k_y^{(B)} = 2p_y - k_y^{(A)}$ stays within $[-k_y^{(0)}, k_y^{(0)}]$. This difference in the integration range subsequently generates the dependence of $\gamma_i(\mathcal{K}, \xi)$ on p_y and, more generally, on \mathcal{K} . Since many channels with different geometrical restrictions contribute to $\partial \gamma_i(\mathcal{K}, \xi) / \partial \xi$ in Eqs. (4.3), the resultant dependence of $\gamma_i(\mathcal{K}, \xi)$ on the four-dimensional vector \mathcal{K} is complicated and hard to visualize. Because of the strong dependence of $\gamma_i(\mathcal{K}, \xi)$ on \mathcal{K} , it is not possible to describe the 2D system by only three renormalizing charges $\gamma_1(\xi)$, $\gamma_2(\xi)$, and $\gamma_3(\xi)$, as in the 1D case. Instead, it is absolutely necessary to consider an infinite number of the renormalizing charges $\gamma_i(\mathcal{K}, \xi)$ labeled by the continuous variable \mathcal{K} . This important difference was neglected in Ref. [7], where the continuous variable \mathcal{K} was omitted.

Having calculated $\gamma_i(\mathcal{K}, \xi)$, we solve Eqs. (4.7) and (4.12) for the triangular vertices (the order parameters) $\mathcal{T}(k_y, q_y, \xi)$, which depend on both the relative (k_y) and the total (q_y) transverse momenta. We find numerically that the order parameters with $q_y = 0$ diverge faster than those with $q_y \neq 0$. This is a natural consequence of the integration range restrictions discussed above. For this reason, we discuss below only the order parameters with zero total momentum $q_y = 0$. We select the initial conditions for the symmetric and antisymmetric order parameters in the form:

$$\mathcal{T}_i^+(k_y, \xi=0) = 1, \quad \mathcal{T}_i^-(k_y, \xi=0) = k_y. \quad (5.1)$$

In Figs. 13 and 14, we present typical dependences of the superconducting and density-wave order parameters on the relative momentum k_y at the same renormalization “time” $\xi = 1.4$ as in Fig. 12. The singlet antisymmetric component (\mathcal{T}_{SSC}^-) dominates among the superconducting order parameters (Fig. 13), whereas the symmetric SDW order parameter (\mathcal{T}_{SDW}^+) is the highest in the density-wave channel (Fig. 14).

Having calculated the triangular vertices \mathcal{T} , we find the susceptibilities from Eq. (4.16). The results are shown in Fig. 15. The symmetric SDW has the fastest growing susceptibility χ_{SDW}^+ , which diverges at $\xi_{SDW} = 1.76$. This divergence indicates that a phase transition from the metallic to the antiferromagnetic state takes place at the transition temperature $T_{SDW} = \mu \exp(-2\pi v_F \xi_{SDW}/g)$. A similar result was obtained in Ref. [29] by analyzing the convergence radius of the parquet series in powers of $g\xi$. In the ladder approximation, the SDW instability would take place at $\xi_{SDW}^{\text{lad}} = 1/g_2 = 1$, as follows from Eqs. (4.14) and (4.18c). Since $\xi_{SDW} > \xi_{SDW}^{\text{lad}}$, the transition temperature T_{SDW} , calculated in the parquet approximation, is lower than the temperature T_{SDW}^{lad} , calculated in the ladder approximation: $T_{SDW} < T_{SDW}^{\text{lad}}$. The parquet temperature is lower, because competing superconducting and density-wave instabilities partially suppress each other.

Thus far, we considered the model with ideally flat regions on the Fermi surface. Suppose now that these regions are only approximately flat. That is, they can be treated as being flat for the energies higher than a certain value E_{cutoff} , but a curvature or a corrugation of the Fermi surface becomes appreciable at the smaller energies $E < E_{\text{cutoff}}$. Because of the curvature, the Fermi surface does not have nesting for $E < E_{\text{cutoff}}$; thus, the density-wave bricks in the parquet equations (4.3) stop to renormalize. Formally, this effect can be taken into account by introducing a cutoff $\xi_{\text{cutoff}} = (1/2\pi v_F) \ln(\mu/E_{\text{cutoff}})$, so that the r.h.s. of Eqs. (4.3c)–(4.3f) for the density-wave bricks are replaced by zeros at $\xi > \xi_{\text{cutoff}}$. At the same time, Eqs. (4.3a) and (4.3b) for the superconducting bricks remain unchanged, because the curvature of the Fermi surface does not affect the superconducting instability with $q_y = 0$. The change of the renormalization equations at ξ_{cutoff} is not a completely rigorous way [38] to take into account the Fermi surface curvature; however, this procedure permits obtaining explicit results and has a certain qualitative appeal. For a more rigorous treatment of the corrugated Fermi surface problem see Ref. [39].

In Fig. 16, we show the susceptibilities calculated using the cutoff procedure with $\xi_{\text{cutoff}} = 1.4$. The density-wave susceptibilities remain constant at $\xi > \xi_{\text{cutoff}}$. At the same time, $\chi_{\text{SSC}}^-(\xi)$ diverges at $\xi_{\text{SSC}}^- = 2.44$ indicating a transition into the singlet superconducting state of the d -wave type. Thus, if the SDW instability is suppressed, the system is unstable against formation of the d -wave superconductivity. This result is in agreement with the conclusions of Refs. [25,30,32].

From our numerical results, we deduce that the dependence of ξ_{SSC}^- on ξ_{cutoff} is linear: $\xi_{\text{SSC}}^- = a - b \xi_{\text{cutoff}}$ with $b = 2.06$, as shown in the inset to Fig. 17. Converting ξ into energy in this relation, we find a power law dependence:

$$T_{\text{SSC}}^- \propto \frac{1}{E_{\text{cutoff}}^b}. \quad (5.2)$$

Eq. (5.2) demonstrates that increasing the cutoff energy E_{cutoff} decreases the temperature of the superconducting transition, T_{SSC}^- . Such a relation can be qualitatively understood in the following way. There is no bare interaction in the superconducting d -wave channel in the Hubbard model, so the transition is impossible in the ladder approximation. The growth of the superconducting d -wave correlations is induced by the growth of the SDW correlations, because the two channels are coupled in the parquet equations (4.18). If E_{cutoff} is high, the SDW correlations do not have enough renormalization-group “time” ξ to develop themselves because of the early cutoff of the density-wave channels; thus, T_{SSC}^- is low. Hence, decreasing E_{cutoff} increases T_{SSC}^- . However, when E_{cutoff} becomes lower than T_{SDW} , the SDW instability overtakes the superconducting one. Corresponding phase diagram is shown in Fig. 17. Generally speaking, the phase diagram plotted in the energy variables, as opposed to the logarithmic variables ξ , may depend on the absolute value of the bare interaction constant $|g|$. In Fig. 17, we placed the points for the several values of $g = 0.3, 0.4$, and 0.5 ; the phase boundary does not depend much on the choice of g . The phase diagram of Fig. 17 qualitatively resembles the experimental one for the high- T_c superconductors, where transitions between the metallic, antiferromagnetic, and superconducting states are observed. The value of E_{cutoff} may be related to the doping level, which controls the shape of the Fermi surface. Taking into account the crudeness of our approximations, detailed agreement with the experiment should not be expected.

We perform the same calculations also for the Hubbard model with umklapp scattering ($g_1 = g_2 = g_3 = 1$). As one can see in Fig. 18, where the susceptibilities are shown, the umklapp process does not modify the qualitative picture. The leading instability remains the SDW of the symmetric type, which is now also symmetric with respect to the umklapp scattering, whereas the next leading instability is the singlet d -wave superconductivity. The SDW has a phase transition at $\xi_{\text{SDW+}}^+ = 0.54$, which is close to the ladder result $\xi_{\text{SDW+}}^{\text{lad}} = 1/(g_2 + g_3) = 0.5$. Some of the susceptibilities in Fig. 18 coincide exactly, which is a consequence of a special $\text{SU}(2) \times \text{SU}(2)$ symmetry of the Hubbard model at the half filling [40]. The phase diagram with the energy cutoff (Fig. 19) is similar to the one without umklapp (Fig. 17), but the presence of the umklapp scattering decreases the transition temperature of the d -wave superconductivity.

An important issue in the study of the 1D electron gas is the so-called g -ology phase diagram, which was constructed for the first time by Dzyaloshinskii and Larkin [16]. They found that, in some regions of the (g_1, g_2, g_3) space, the 1D electron system develops a charge or spin gap, which is indicated by divergence of $\gamma_i(\xi)$ with increasing ξ . In the region where none of the gaps develops, the Luttinger liquid exists. It is interesting whether such a region may exist in our 2D model. To study the phase diagram of the 2D system, we repeat the calculations, systematically changing relative values of g_1 , g_2 , and g_3 . From the physical point of view, the relative difference of g_1 , g_2 , and g_3 roughly mimics dependence of the interaction vertex on the momentum transfer. As an example, we show the susceptibilities in the case where $g_1 = 2$, $g_2 = 1$, and $g_3 = 0$ in Fig. 20. In this case, the leading instabilities are simultaneously the triplet superconductivity of the symmetric type (TSC+) and the spin-density wave.

For all studied sets of g_i , we find that the leading instabilities calculated in the parquet and the ladder approximations always coincide. (We do not introduce the energy cutoff here.) Thus, the parquet effects do not modify the g -ology phase diagram of the 2D model derived in the ladder approximation, even though the transition temperatures

in the parquet approximation are always lower than those obtained in the ladder approximation. In that sense, the parquet corrections are much less important in the 2D case than in the 1D case. From the mathematical point of view, this happens because a leading divergent brick develops a strong dependence on the transverse momenta \mathcal{K} and acquires the so-called mobile pole structure [20,22,29]:

$$Z(\mathcal{K}, \xi) \propto \frac{1}{\xi_c(\mathcal{K}) - \xi}. \quad (5.3)$$

The name “mobile pole” is given, because the position of the pole in ξ in Eq. (5.3), $\xi_c(\mathcal{K})$, strongly depends on the momenta \mathcal{K} . It was shown in Refs. [22,20,29] that, because of the mobility of the pole, the leading channel decouples from the other channels, and the parquet description effectively reduces to the ladder one, as described at the end of Sec. IV. The phase diagram of the 2D system in the ladder approximation is given by Eqs. (4.21). It follows from Eqs. (4.21) that every point in the (g_1, g_2, g_3) space has some sort of instability. Thus, the Luttinger liquid, defined as a nontrivial metallic ground state where different instabilities mutually cancel each other, does not exist in the 2D model.

Generally speaking, other models may have different types of solutions of the fast parquet equations, such as immobile poles [20] or a self-similar solution [23], the latter indeed describing some sort of a Luttinger liquid. In our study of a 2D model with the van Hove singularities [32], we found a region in the g -space without instabilities, where the Luttinger liquid may exist [41]. However, we find only the mobile-pole solutions in the present 2D model.

VI. CONCLUSIONS

In this paper we derive and numerically solve the parquet equations for the 2D electron gas whose Fermi surface contains flat regions. The model is a natural generalization of the 1D electron gas model, where the Luttinger liquid is known to exist. We find that, because of the finite size of the flat regions, the 2D parquet equations always develop the mobile pole solutions, where the leading instability effectively decouples from the other channels. Thus, a ladder approximation is qualitatively (but not necessarily quantitatively) correct for the 2D model, in contrast to the 1D case. Whatever the values of the bare interaction constants are, the 2D system always develops some sort of instability. Thus, the Luttinger liquid, defined as a nontrivial metallic ground state where different instabilities mutually cancel each other, does not exist in the 2D model, contrary to the conclusions of Refs. [26,27].

In the case of the repulsive Hubbard model, the leading instability is the SDW, i.e., antiferromagnetism [29]. If the nesting of the Fermi surface is not perfect, the SDW correlations do not develop into a phase transition, and the singlet superconductivity of the d -wave type appears in the system instead. These results may be relevant for the high- T_c superconductors and are in qualitative agreement with the findings of Refs. [25,30,32].

In the bosonization procedure [4–11], a higher-dimensional Fermi surface is treated as a collection of flat patches. Since the results of our paper do not depend qualitatively on the size of the flat regions on the Fermi surface, the results may be applicable, to some extent, to the patches as well. Precise relation is hard to establish because of the infinitesimal size of the patches, their different orientations, and uncertainties of connections between them. On the other hand, the bosonization procedure seems to be even better applicable to a flat Fermi surface, which consists of a few big patches. Mattis [26] and Hlubina [27] followed that logic and claimed that the flat Fermi surface model is exactly solvable by the bosonization and represents a Luttinger liquid. The discrepancy between this claim and the results our paper indicates that some conditions must restrict the validity of the bosonization approximations. Luther gave a more sophisticated treatment to the flat Fermi surface problem by mapping it onto multiple quantum chains [28]. He found that the bosonization converts the interaction between electrons into the two types of terms, roughly corresponding to the two terms of the sine-Gordon model: the “harmonic” terms $(\partial\varphi/\partial x)^2$ and the “exponential” terms $\exp(i\varphi)$, where φ is a bosonization phase. The harmonic terms can be readily diagonalized, but the exponential terms require a consistent renormalization-group treatment. If the renormalization-group equations were derived in the bosonization scheme of [28], they would be the same as the parquet equations written in our paper, because the renormalization-group equations do not depend on whether the boson or fermion representation is used in their derivation [42].

Long time ago, Luther bosonized noninteracting electrons on a curved Fermi surface [43]; however, the interaction between the electrons remained intractable because of the exponential terms. The recent bosonization in higher dimensions [4–11] managed to reformulate the problem in the harmonic terms only. This is certainly sufficient to reproduce the Landau description of sound excitations in a Fermi liquid [44]; however, it may be not sufficient to derive the electron correlation functions. The validity of the harmonic approximation is hard to trace for a curved Fermi surface, but considerable experience has been accumulated for the flat Fermi surface models.

In the model of multiple 1D chains without single-electron tunneling between the chains and with forward scattering between different chains, the bosonization produces the harmonic terms only, thus the model can be solved exactly [19,45]. However, a slight modification of the model by introducing backward scattering between different chains [20,46] or interaction between four different chains [21] adds the exponential terms, which destroy the exact solvability and typically lead to a CDW or SDW instability. Even if no instability occurs, as in the model of electrons in a high magnetic field [23], the fast parquet method shows that the electron correlation functions have a complicated, nonpower structure, which is impossible to obtain within the harmonic bosonization. Further comparison of the fast parquet method and the bosonization in higher dimensions might help to establish the conditions of applicability of the two complementary methods.

The work at Maryland was partially supported by the NSF under Grant DMR-9417451, by the Alfred P. Sloan Foundation, and by the David and Lucile Packard Foundation.

* E-mail anatoley@glue.umd.edu

† E-mail yakovenk@glue.umd.edu

- [1] Yu. A. Firsov, V. N. Prigodin, and Chr. Seidel, *Phys. Repts.* **126**, 245 (1985).
- [2] F. D. M. Haldane, *J. Phys. C* **14**, 2585 (1981).
- [3] P. W. Anderson, *Physica Scripta T* **42**, 11 (1992).
- [4] F. D. M. Haldane, in *Perspectives in Many-Particle Physics*, Proceedings of the International School of Physics “Enrico Fermi,” course 121, Varenna, 1992, edited by R. Schrieffer and R. A. Broglia (North-Holland, New York, 1994).
- [5] D. V. Khveshchenko, R. Hlubina, and T. M. Rice, *Phys. Rev. B* **48**, 10766 (1993); D. V. Khveshchenko and P. C. E. Stamp, *Phys. Rev. Lett.* **71**, 2118 (1993); *Phys. Rev. B* **49**, 5227 (1994); D. V. Khveshchenko, *Phys. Rev. B* **52**, 4833 (1995) [cond-mat/9409118].
- [6] D. V. Khveshchenko, *Phys. Rev. B* **49**, 16893 (1994) [cond-mat/9401012].
- [7] A. Houghton and J. B. Marston, *Phys. Rev. B* **48**, 7790 (1993) [cond-mat/9210007].
- [8] A. Houghton, H.-J. Kwon, and J. B. Marston, *Phys. Rev. B* **50**, 1351 (1994) [cond-mat/9310043]; A. Houghton, H.-J. Kwon, J. B. Marston, and R. Shankar, *J. Phys. Cond. Mat.* **6**, 4909 (1994) [cond-mat/9312067]; H.-J. Kwon, A. Houghton, and J. B. Marston, *Phys. Rev. Lett.* **73**, 284 (1994) [cond-mat/9401041]; *Phys. Rev. B* **52**, 8002 (1995) [cond-mat/9501067].
- [9] A. H. C. Neto and E. Fradkin, *Phys. Rev. Lett.* **72**, 1393 (1994) [cond-mat/9304014]; *Phys. Rev. B* **49**, 10877 (1994) [cond-mat/9307005]; *Phys. Rev. B* **51**, 4084 (1995) [cond-mat/9310046].
- [10] Y. M. Li, *Phys. Rev. B* **51**, 13046 (1995).
- [11] P. Kopietz, J. Hermisson, and K. Schonhammer, *Phys. Rev. B* **52**, 10877 (1995) [cond-mat/9304014]; P. Kopietz, *Phys. Rev. B* **53**, 12761 (1996) [cond-mat/9503090]; P. Kopietz and G. E. Castilla, *Phys. Rev. Lett.* **76**, 4777 (1996) [cond-mat/9603158].
- [12] R. Shankar, *Rev. Mod. Phys.* **66**, 129 (1994) [cond-mat/9307009].
- [13] J. Solyom, *Adv. Phys.* **28**, 201 (1979).
- [14] I. T. Diatlov, V. V. Sudakov, and K. A. Ter-Martirosian, *Zh. Exp. Teor. Fiz.* **32**, 767 (1957) [Sov. Phys. JETP **5**, 631 (1957)]; V. V. Sudakov, *Dokl. Akad. Nauk SSSR* **111**, 338 (1956) [Sov. Phys. Doklady **1**, 662 (1957)].
- [15] Y. A. Bychkov, L. P. Gor’kov, and I. E. Dzyaloshinskii, *Zh. Exp. Teor. Fiz.* **50**, 738 (1966) [Sov. Phys. JETP **23**, 489 (1966)].
- [16] I. E. Dzyaloshinskii and A. I. Larkin, *Zh. Exp. Teor. Fiz.* **61**, 791 (1972) [Sov. Phys. JETP **34**, 422 (1972)].
- [17] A. A. Abrikosov, *Physics* **2**, 5 (1965).
- [18] B. Roulet, J. Gavoret, and P. Nozières, *Phys. Rev.* **178**, 1072 (1969); P. Nozières, J. Gavoret, and B. Roulet, *Phys. Rev.* **178**, 1084 (1969).
- [19] I. E. Dzyaloshinskii and A. I. Larkin, *Zh. Exp. Teor. Fiz.* **65**, 411 (1973) [Sov. Phys. JETP **38**, 202 (1973)].
- [20] L. P. Gor’kov and I. E. Dzyaloshinskii, *Zh. Exp. Teor. Fiz.* **67**, 397 (1974) [Sov. Phys. JETP **40**, 198 (1975)].
- [21] V. M. Yakovenko, *Zh. Exp. Teor. Fiz.* **93**, 627 (1987) [Sov. Phys. JETP **66**, 355 (1987)]; *Phys. Rev. B* **43**, 11353 (1991).
- [22] S. A. Brazovskii, *Zh. Exp. Teor. Fiz.* **61**, 2401 (1971); **62**, 820 (1972) [Sov. Phys. JETP **34**, 1286 (1972); **35**, 433 (1972)];
- [23] V. M. Yakovenko, *Phys. Rev. B* **47**, 8851 (1993) [cond-mat/9205008].
- [24] A. Virosztek and J. Ruvalds, *Phys. Rev. B* **42**, 4064 (1990).
- [25] J. Ruvalds *et al.*, *Phys. Rev. B* **51**, 3797 (1995) [cond-mat/9403013].
- [26] D. C. Mattis, *Phys. Rev. B* **36**, 745 (1987).
- [27] R. Hlubina, *Phys. Rev. B* **50**, 8252 (1994) [cond-mat/9312083].
- [28] A. Luther, *Phys. Rev. B* **50**, 11446 (1994) [cond-mat/9405046].
- [29] I. E. Dzyaloshinskii and E. I. Kats, *Zh. Exp. Teor. Fiz.* **62**, 1104 (1972) [Sov. Phys. JETP **35**, 584 (1972)].
- [30] D. J. Scalapino, J. E. Loh, and J. E. Hirsch, *Phys. Rev. B* **34**, 8190 (1986); *Phys. Rev. B* **35**, 6694 (1987).

- [31] B. G. Levi, Phys. Today, January 1996, p. 19; May 1993, p. 17.
- [32] I. E. Dzyaloshinskii, Zh. Exp. Teor. Fiz. **93**, 1487 (1987) [Sov. Phys. JETP **66**, 848 (1987)]; I. E. Dzyaloshinskii and V. M. Yakovenko, Zh. Exp. Teor. Fiz. **94**, 344 (1988) [Sov. Phys. JETP **67**, 844 (1988)]; I. E. Dzyaloshinskii and V. M. Yakovenko, Int. J. Mod. Phys. B **2**, 667 (1988).
- [33] D. S. Dessau *et al.*, Phys. Rev. Lett. **71**, 2781 (1993); Z.-X. Shen *et al.*, Science **267**, 343 (1995).
- [34] A. A. Abrikosov, L. P. Gorkov, and I. E. Dzyaloshinskii, *Methods of Quantum Field Theory in Statistical Physics* (Pergamon, New York, 1975).
- [35] L. D. Landau and E. M. Lifshitz, *Statistical Physics, Part 1* (Pergamon, Oxford, 1993), §163.
- [36] B. Halperin and T. M. Rice, Sol. State Phys. **21**, 115 (1968); A. A. Nersesyan and G. E. Vachnadze, J. Low Temp. Phys. **77**, 293 (1989); H. J. Schulz, Phys. Rev. B **39**, 2940 (1989).
- [37] I. Affleck and J. B. Marston, Phys. Rev. B **37**, 3774 (1988); G. Kotliar, Phys. Rev. B **37**, 3664 (1988).
- [38] G. T. Zimanyi, S. A. Kivelson, and A. Luther, Phys. Rev. Lett. **60**, 2089 (1988).
- [39] V. N. Prigodin and Yu. A. Firsov, Pis'ma Zh. Exp. Teor. Fiz. **25**, 90 (1977) [JETP Lett. **25**, 79 (1977)]; Zh. Exp. Teor. Fiz. **76**, 736 (1979) [Sov. Phys. JETP **49**, 369 (1979)]; Zh. Exp. Teor. Fiz. **76**, 1602 (1979) [Sov. Phys. JETP **49**, 813 (1979)].
- [40] H. J. Schulz, Phys. Rev. Lett. **65**, 2462 (1990); C. N. Yang and S. C. Zhang, Mod. Phys. Lett. B **4**, 759 (1990); M. Pernici, Europhys. Lett. **12**, 75 (1990).
- [41] I. E. Dzyaloshinskii, J. Phys. (Paris) I **6**, 119 (1996).
- [42] P. B. Wiegmann, J. Phys. C **11**, 1583 (1978).
- [43] A. Luther, Phys. Rev. B **19**, 320 (1979).
- [44] E. M. Lifshitz and L. P. Pitaevskii, *Statistical Physics, Part 2* (Pergamon, Oxford, 1991), Chap. 1.
- [45] R. A. Klemm and H. Gutfreund, Phys. Rev. B **14**, 1086 (1976).
- [46] P. A. Lee, T. M. Rice, and R. A. Klemm, Phys. Rev. B **15**, 2984 (1977).

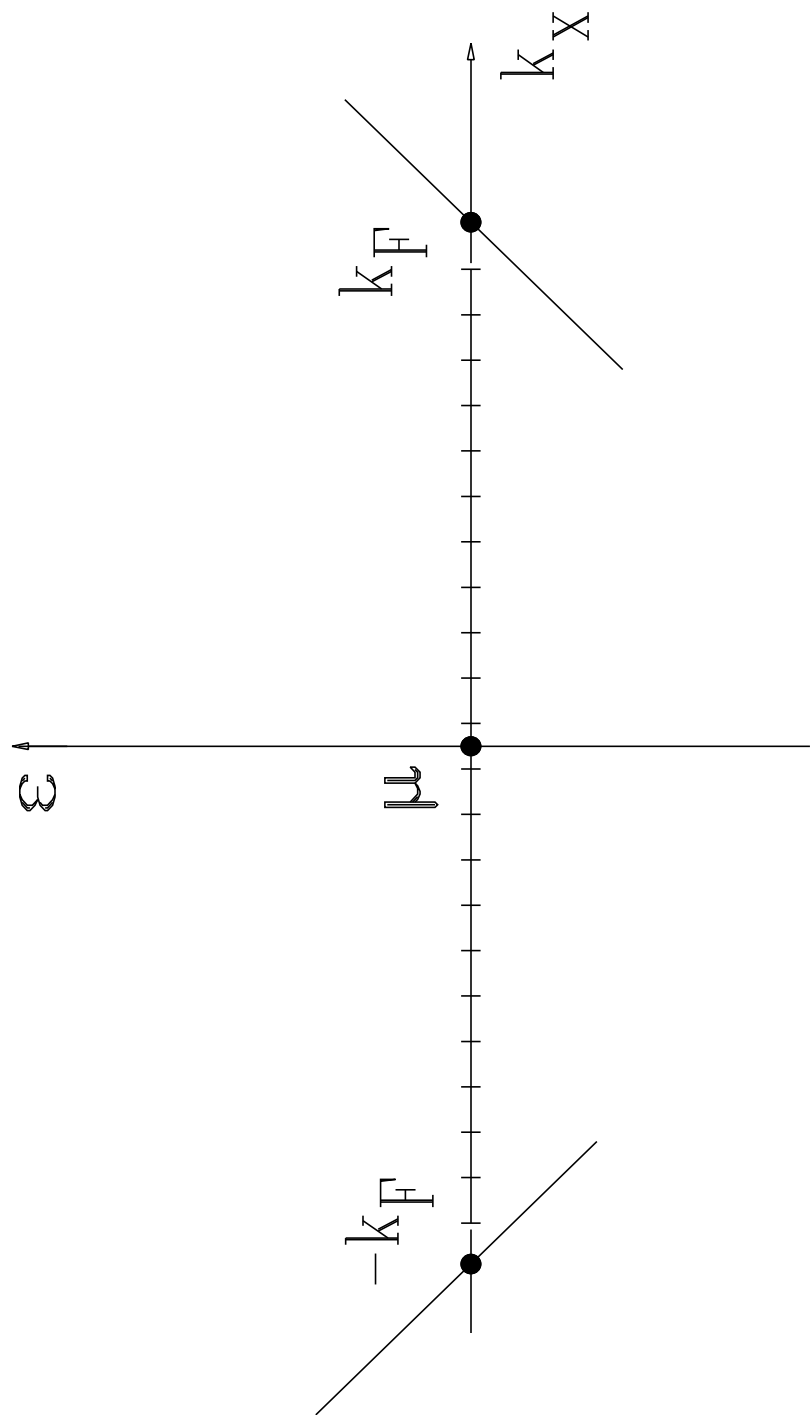


FIG. 1. Dispersion law of 1D electrons. The states in the shaded range of the momentum k_x are occupied by electrons.

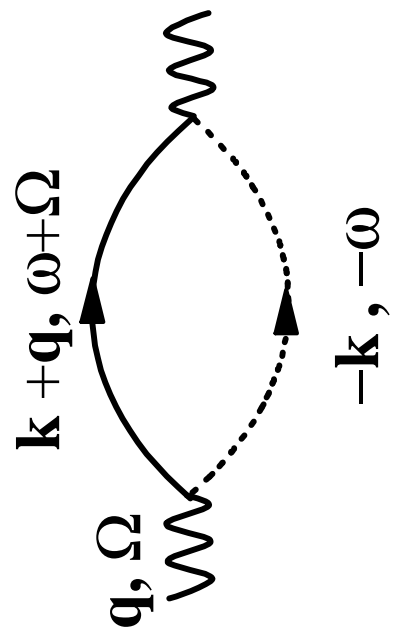
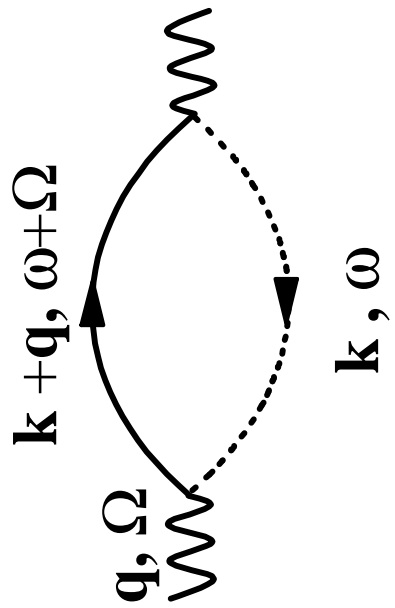


FIG. 2. Bare superconducting and density-wave susceptibilities. The solid and dashed lines represent the Green functions of the + and - electrons. The wavy lines represent incoming momentum and energy.

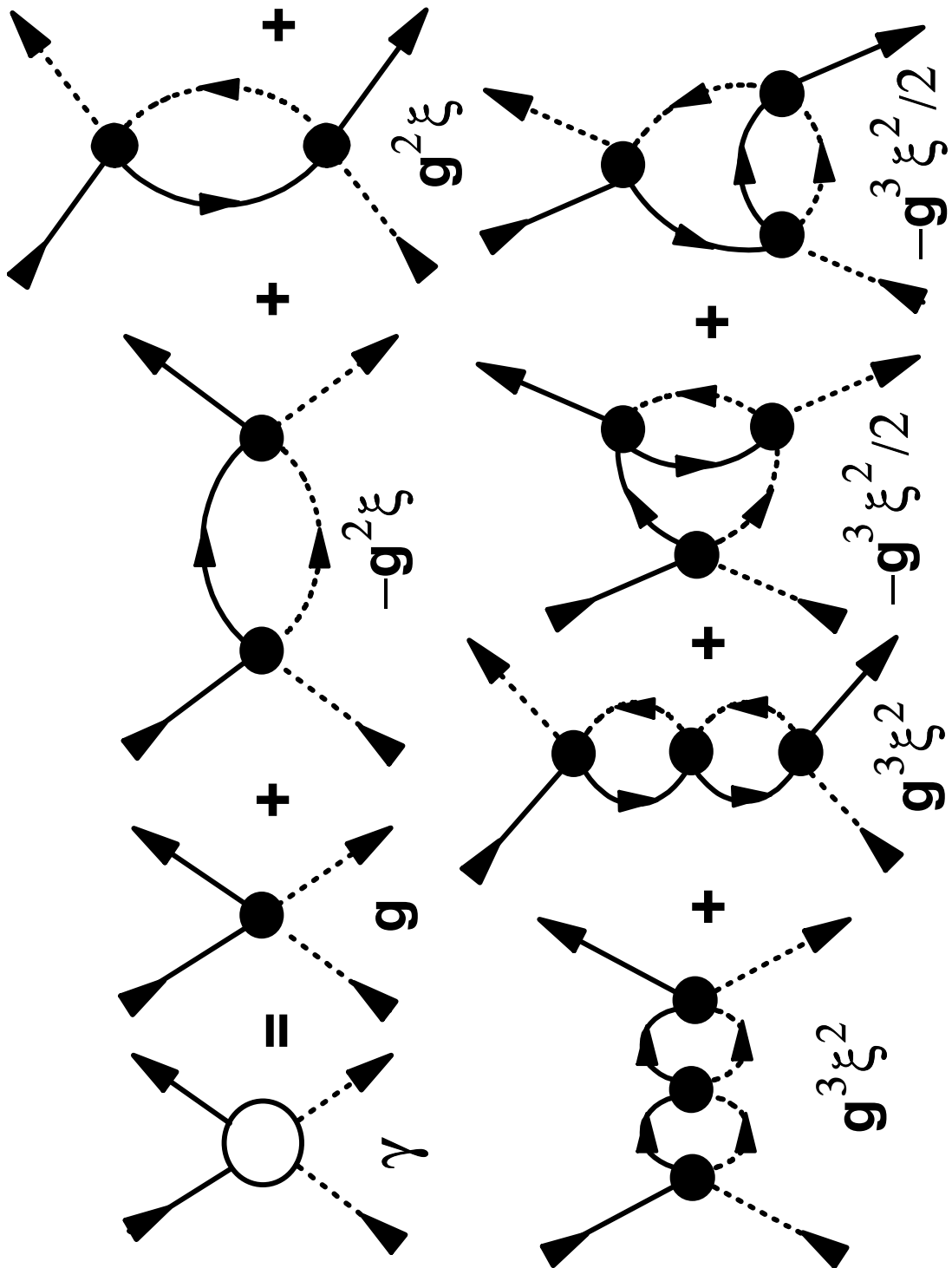


FIG. 3. Some parquet corrections to the vertex of interaction between electrons, γ , which is shown as a circle. The dots represent the bare interaction vertex g . The expressions beneath the diagrams represent the values of the corresponding diagrams.

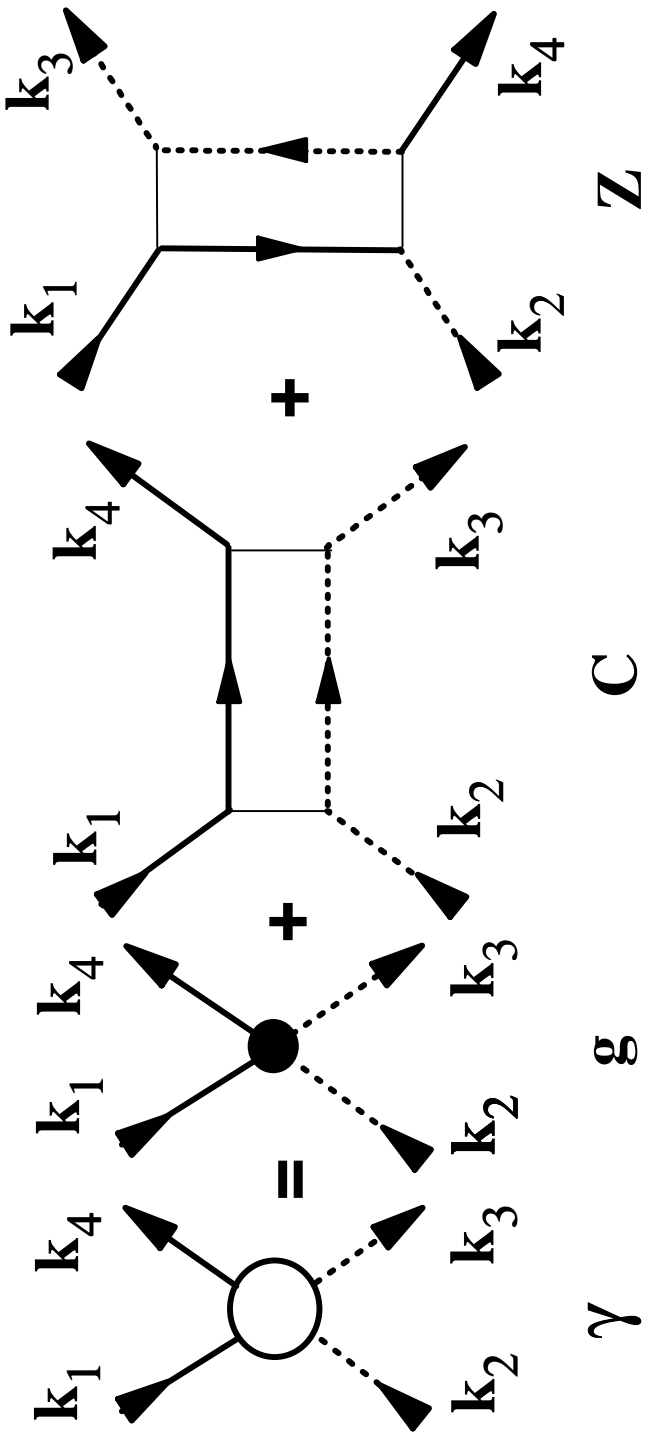
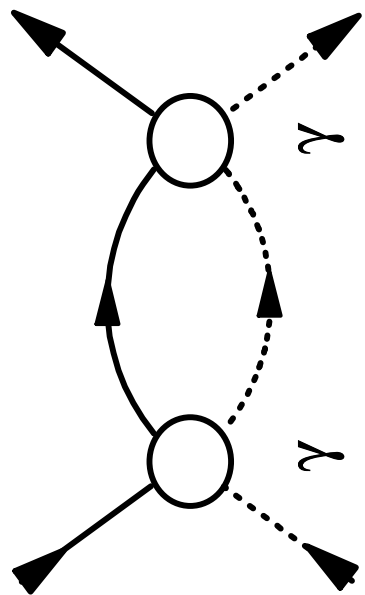
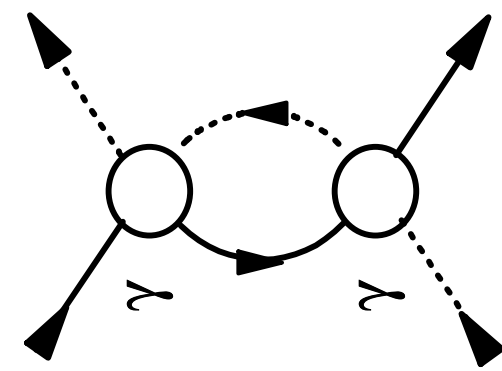


FIG. 4. Decomposition of the interaction vertex γ , shown as a circle, into superconducting and density-wave bricks, shown as rectangles, in the spinless case.



||



||

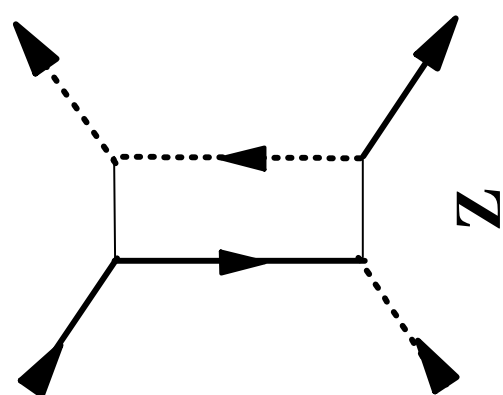
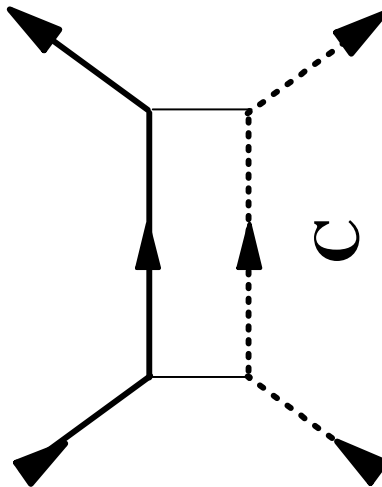
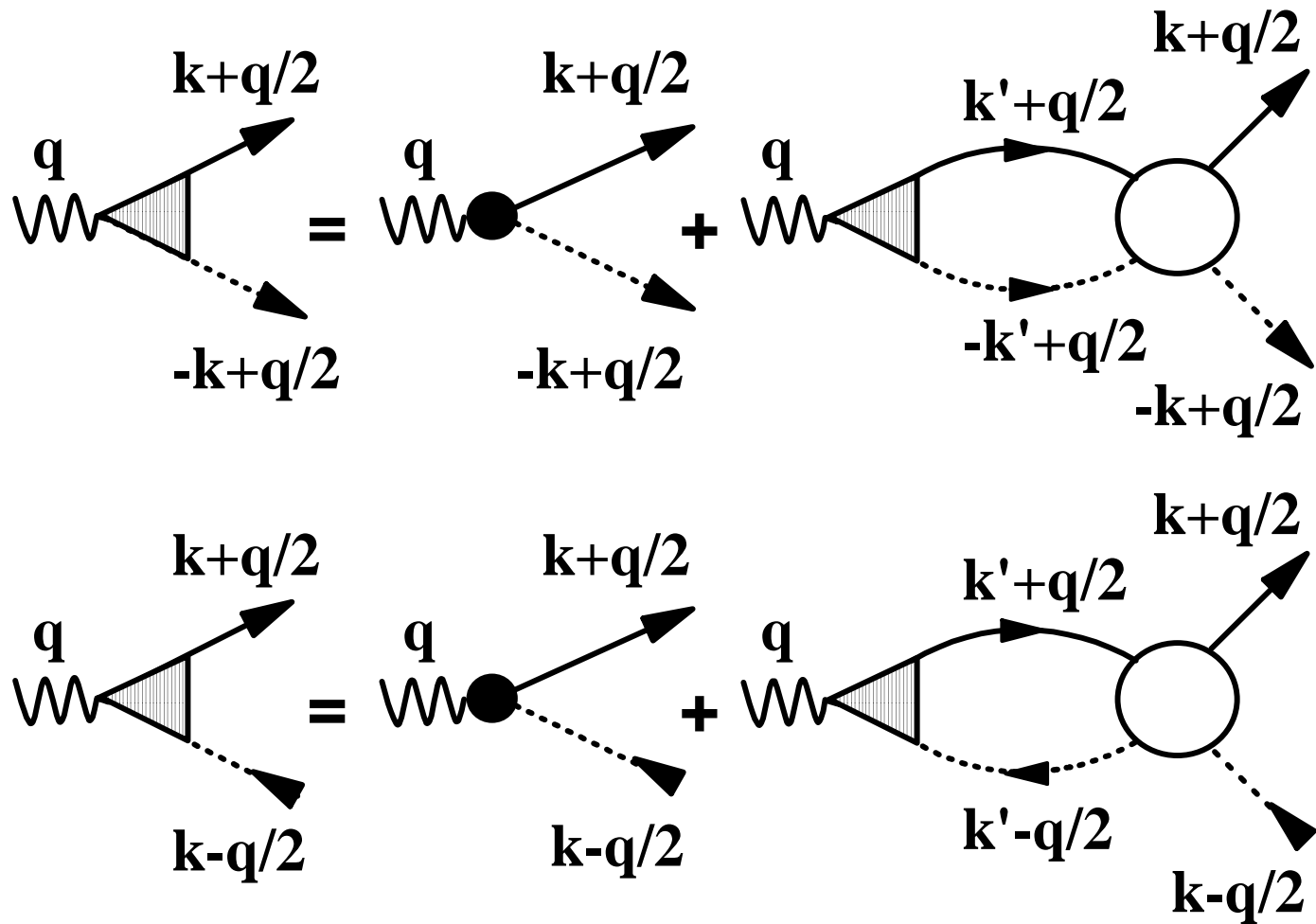


FIG. 5. Parquet equations for the bricks in the spinless case.

FIG. 6. Parquet equations for the triangular vertices in the spinless case. The filled triangles represent the vertices \mathcal{T}_{SC} and \mathcal{T}_{DW} , whereas the dots represent the auxiliary external fields h_{SC} and h_{DW} .



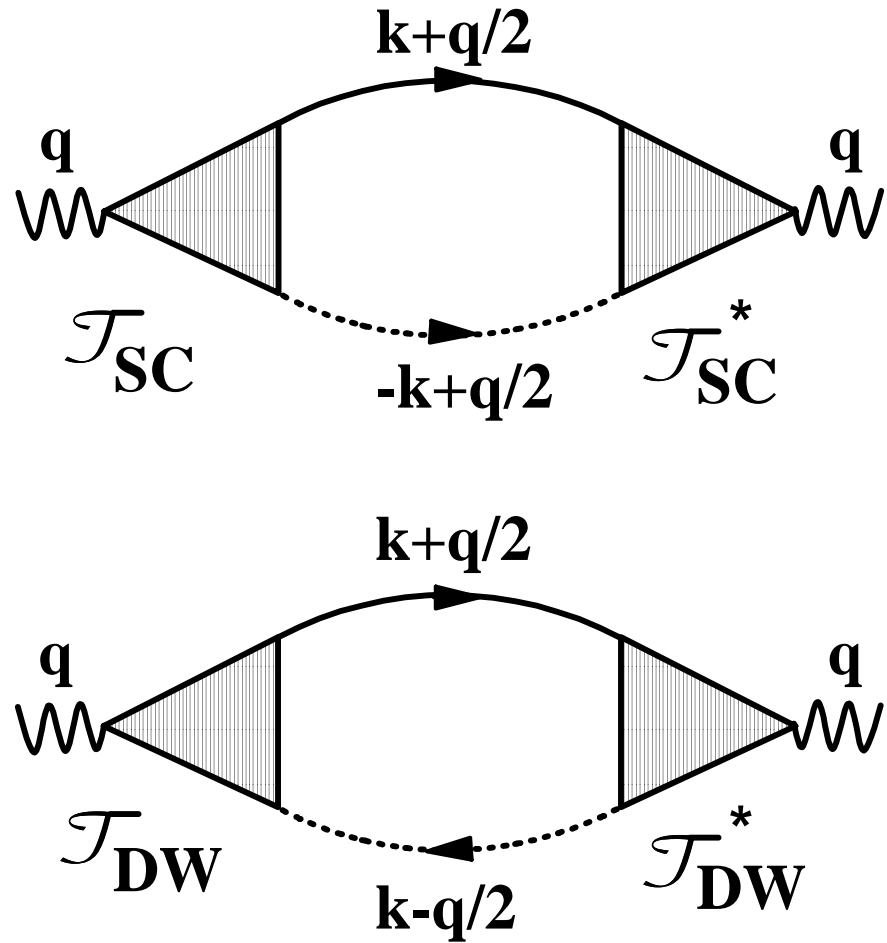


FIG. 7. Parquet equations for the free energy corrections F_{SC} and F_{DW} in the spinless case.

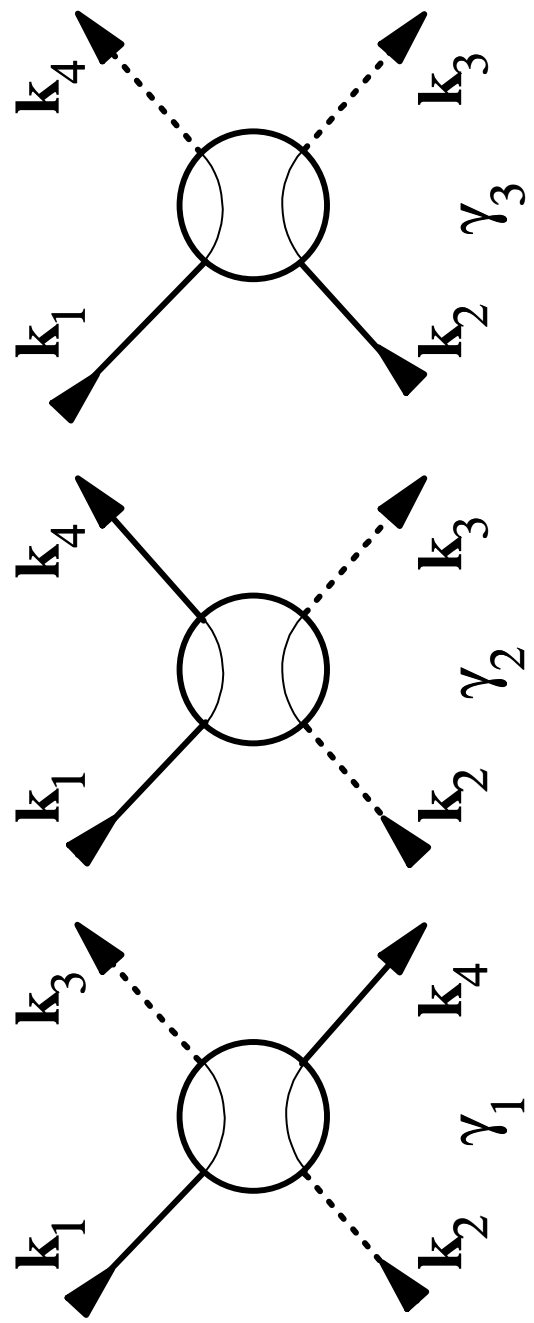
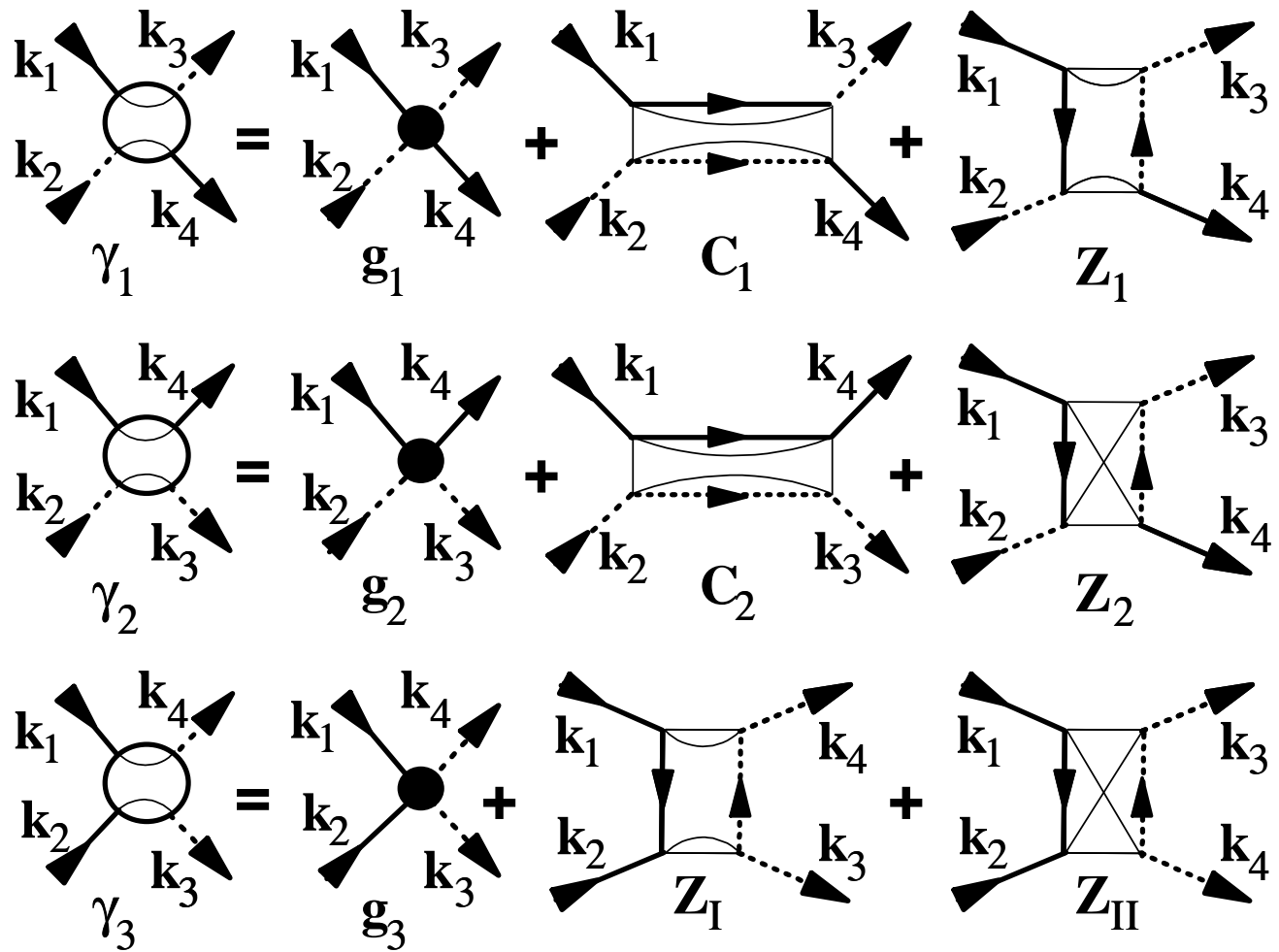


FIG. 8. Vertices of interaction between electrons with spin: backward (γ_1), forward (γ_2), and umklapp (γ_3) scattering. The thin solid lines inside the circles indicate how spin is conserved.

FIG. 9. Decomposition of the interaction vertices (shown as circles) into superconducting and density-wave bricks (shown as rectangles) for electrons with spin. The thin solid lines inside the circles and rectangles indicate how spin is conserved. The dots represent the bare interaction vertices.



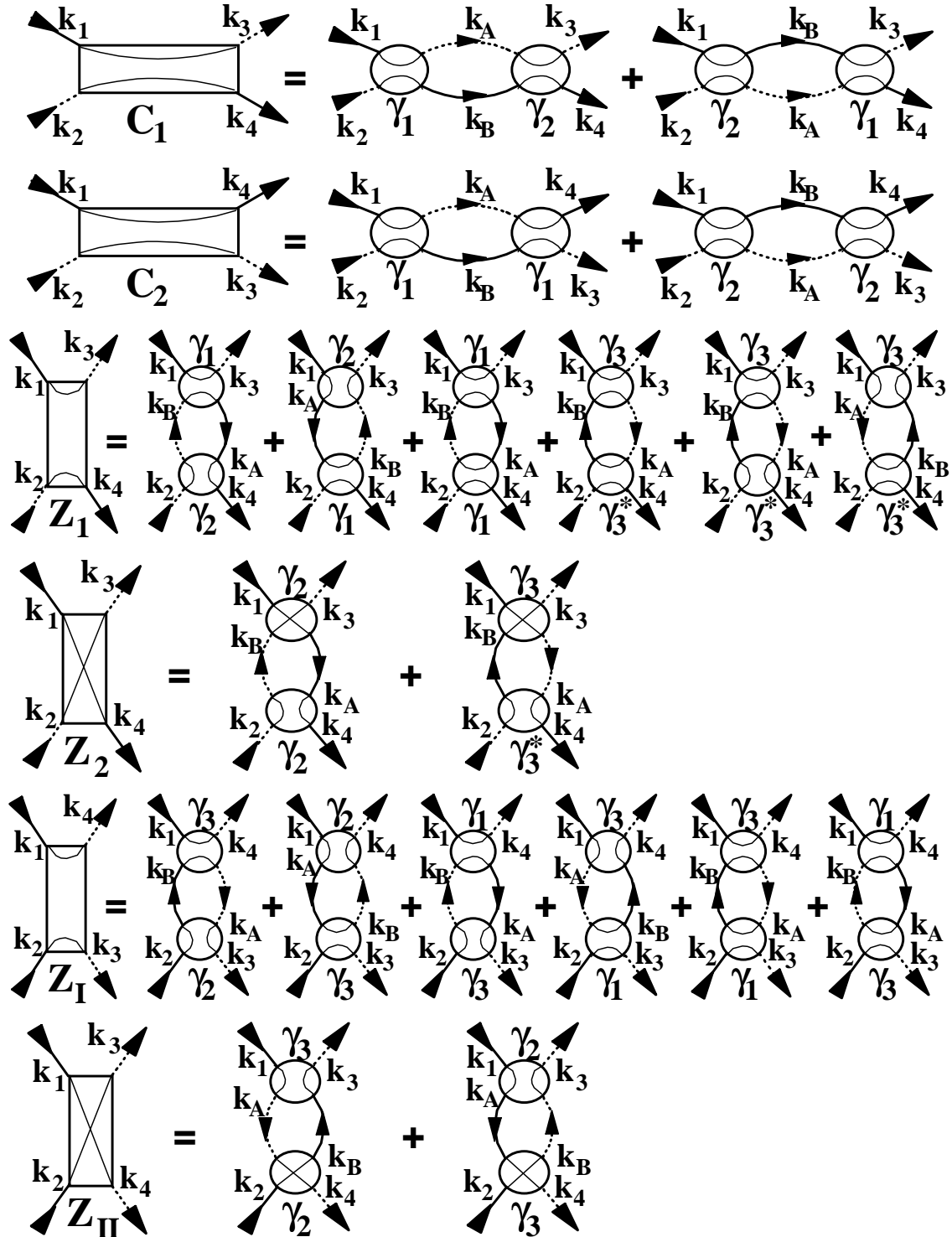


FIG. 10. Parquet equations for the bricks for electrons with spin. The variables k_1 and k_2 (k_3 and k_4) represent momenta of incoming (outgoing) electrons, whereas the variables k_A and k_B represent intermediate momenta that should be integrated over.

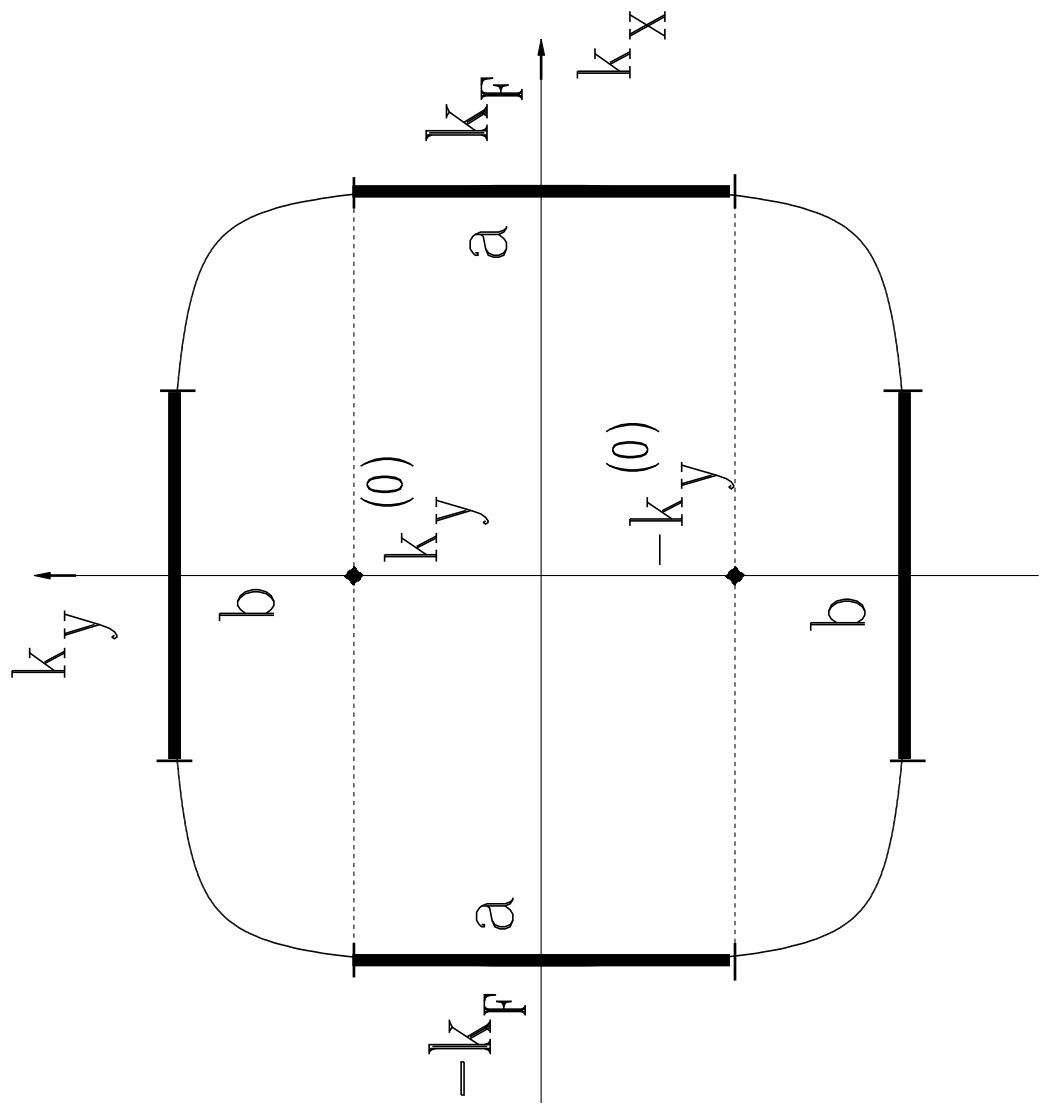


FIG. 11. Fermi surface of a 2D electron gas. The thick lines indicate flat regions on the Fermi surface.

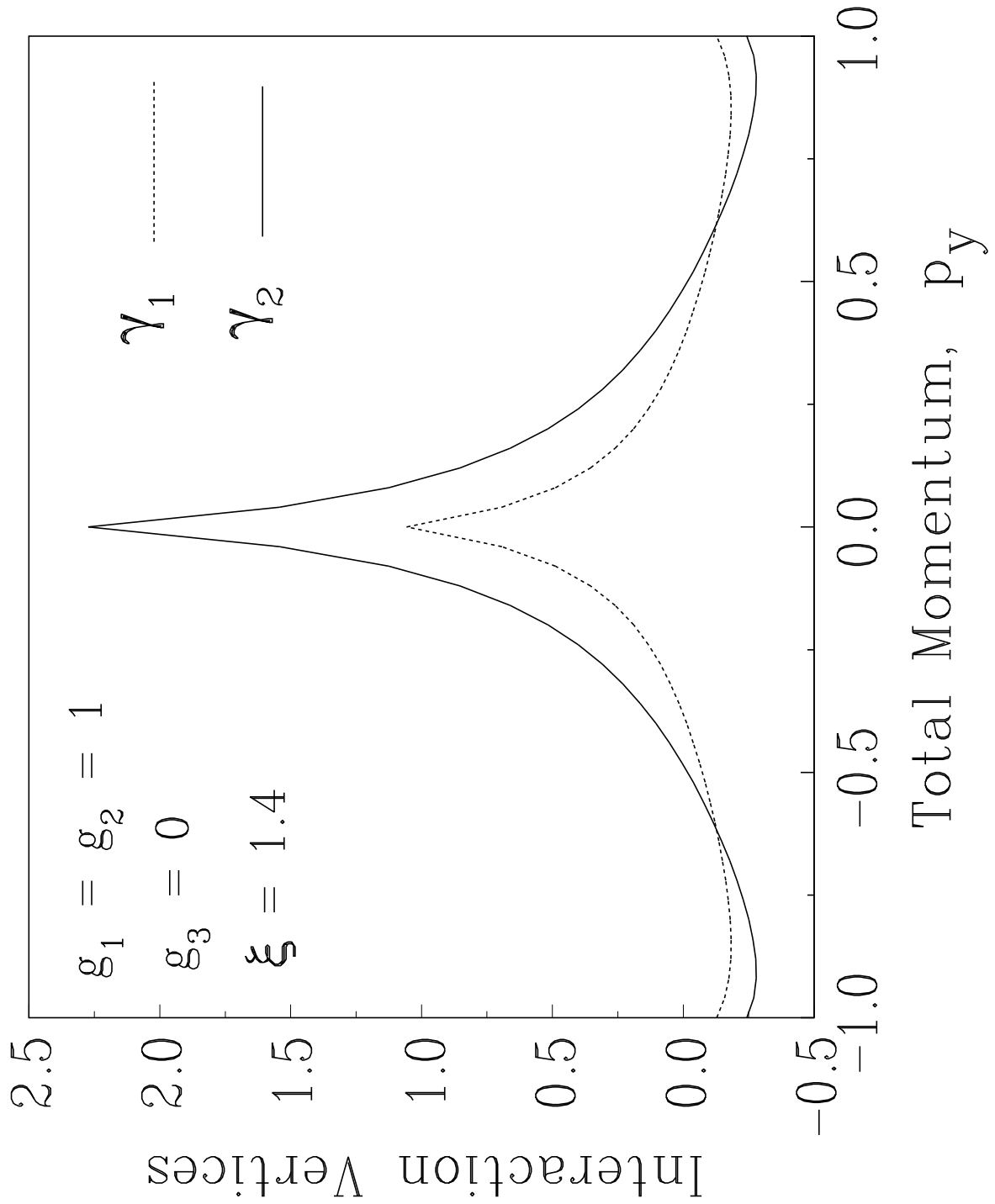


FIG. 12. Interaction vertices $\gamma_1(k_y^{(1)}, k_y^{(2)}; k_y^{(3)}, k_y^{(4)}; \xi)$ and $\gamma_2(k_y^{(1)}, k_y^{(2)}; k_y^{(3)}, k_y^{(4)}; \xi)$ as functions of the average momentum $p_y = (k_y^{(1)} + k_y^{(2)})/2$ of the incoming electrons at $k_y^{(1)} = k_y^{(3)}$, $k_y^{(2)} = k_y^{(4)}$, and $\xi = 1.4$.

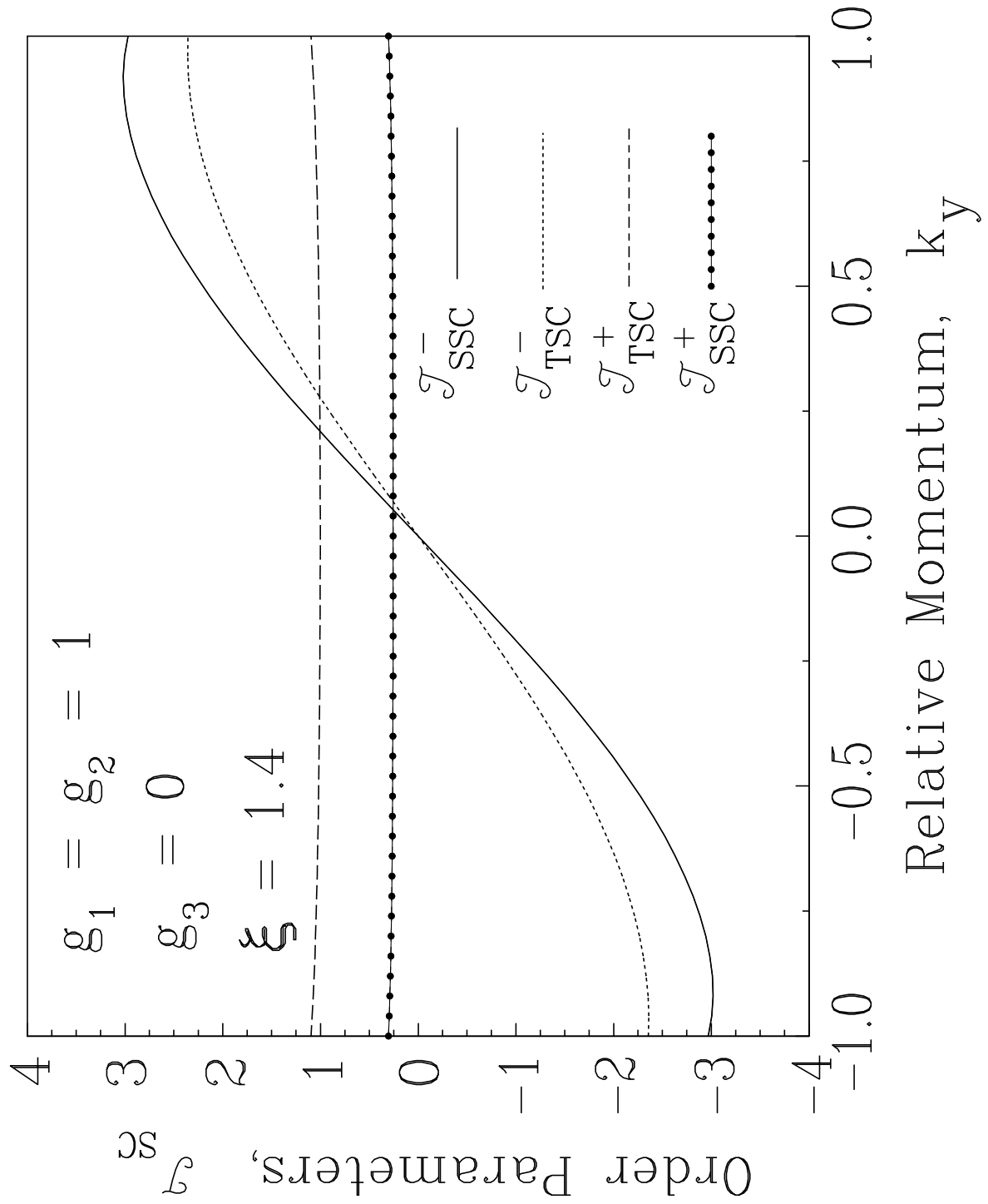


FIG. 13. Superconducting order parameters $T_{SC}(k_y, q_y, \xi)$ as functions of relative momentum k_y at $q_y = 0$ and $\xi = 1.4$.

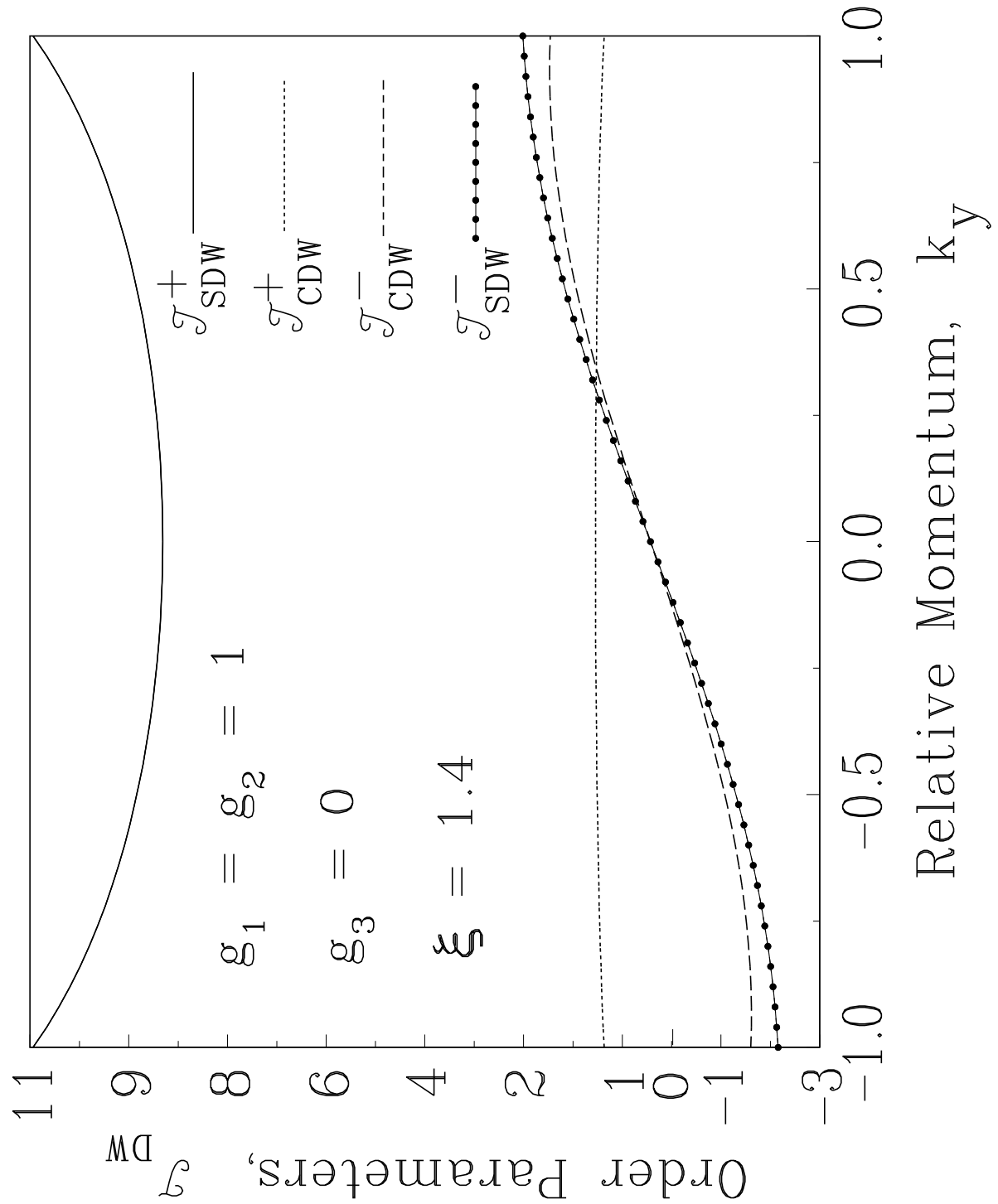


FIG. 14. Density-wave order parameters $T_{DW}(k_y, q_y, \xi)$ as the functions of relative momentum k_y at $q_y = 0$ and $\xi = 1.4$.

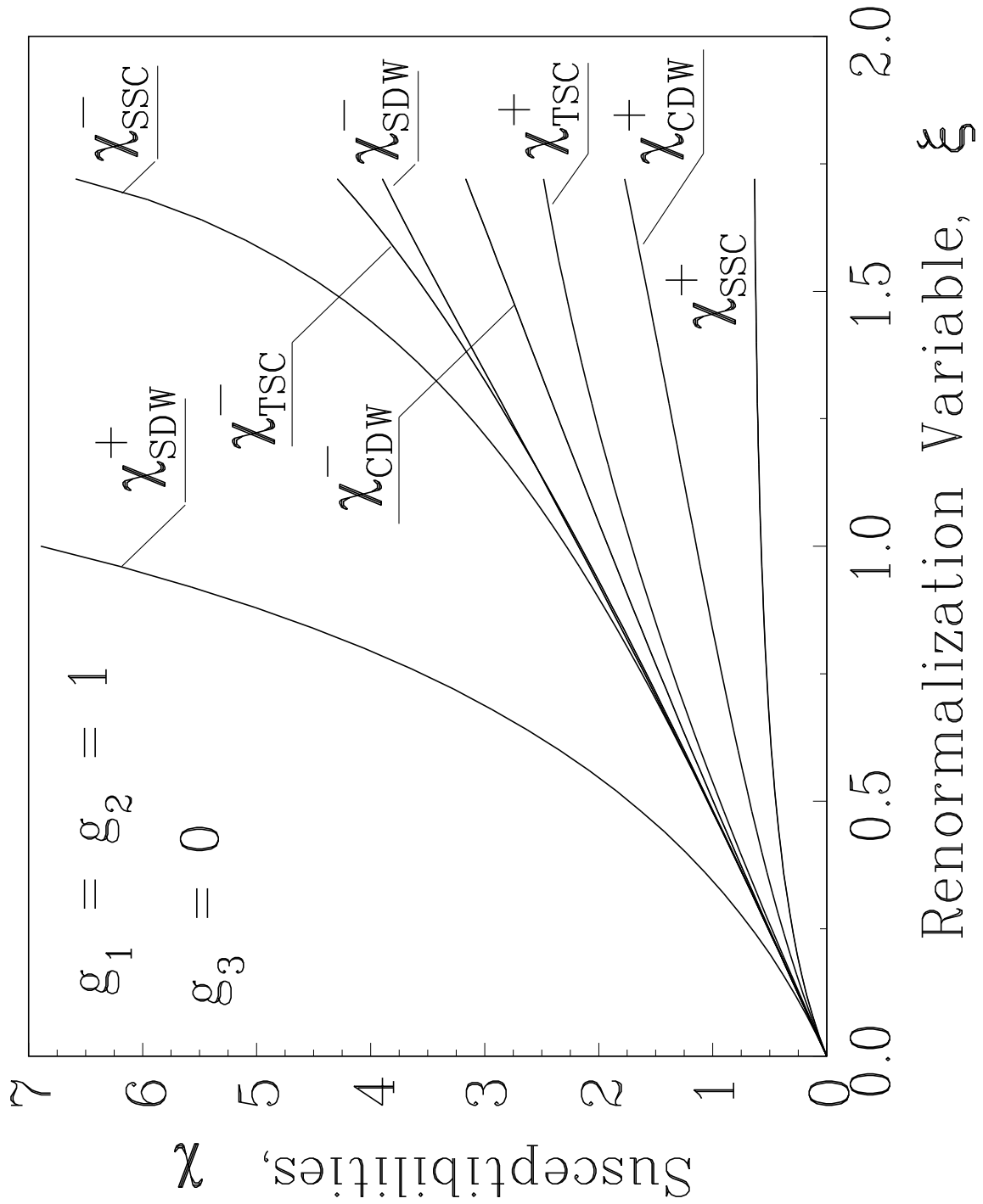


FIG. 15. Evolution of susceptibilities $\chi_i(\xi)$ in the repulsive Hubbard model without umklapp. $\chi_{SDW}^+(\xi)$ diverges at $\xi = \xi_{SDW} = 1.76$.

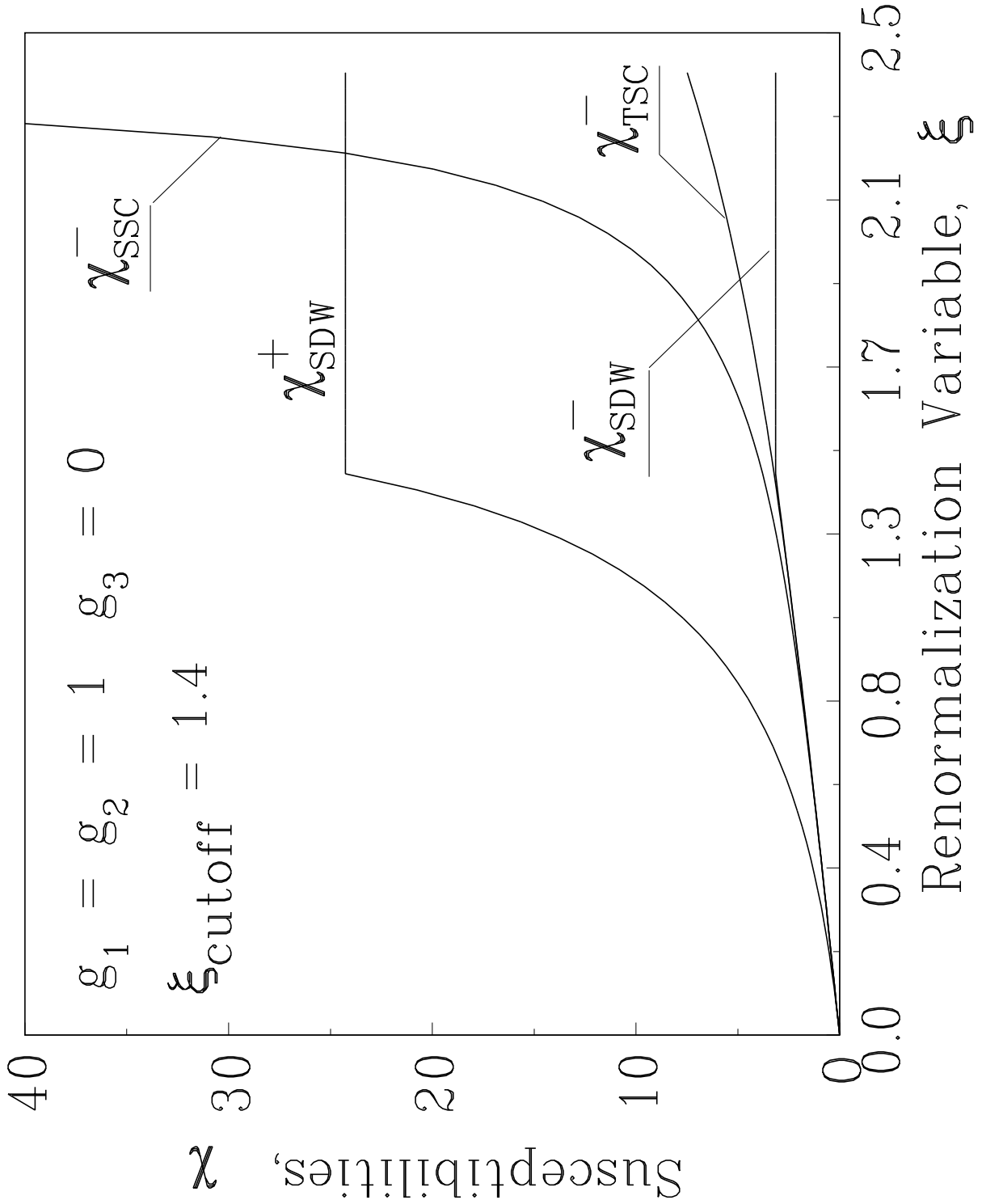


FIG. 16. Evolution of the four leading susceptibilities in the Hubbard model without umklapp, with the cutoff of all density-wave channels at $\xi > \xi_{\text{cutoff}} = 1.4$. The susceptibility of antisymmetric singlet superconductivity, χ^-_{SSC} , diverges at $\xi = \xi^-_{SSC} = 2.44$.

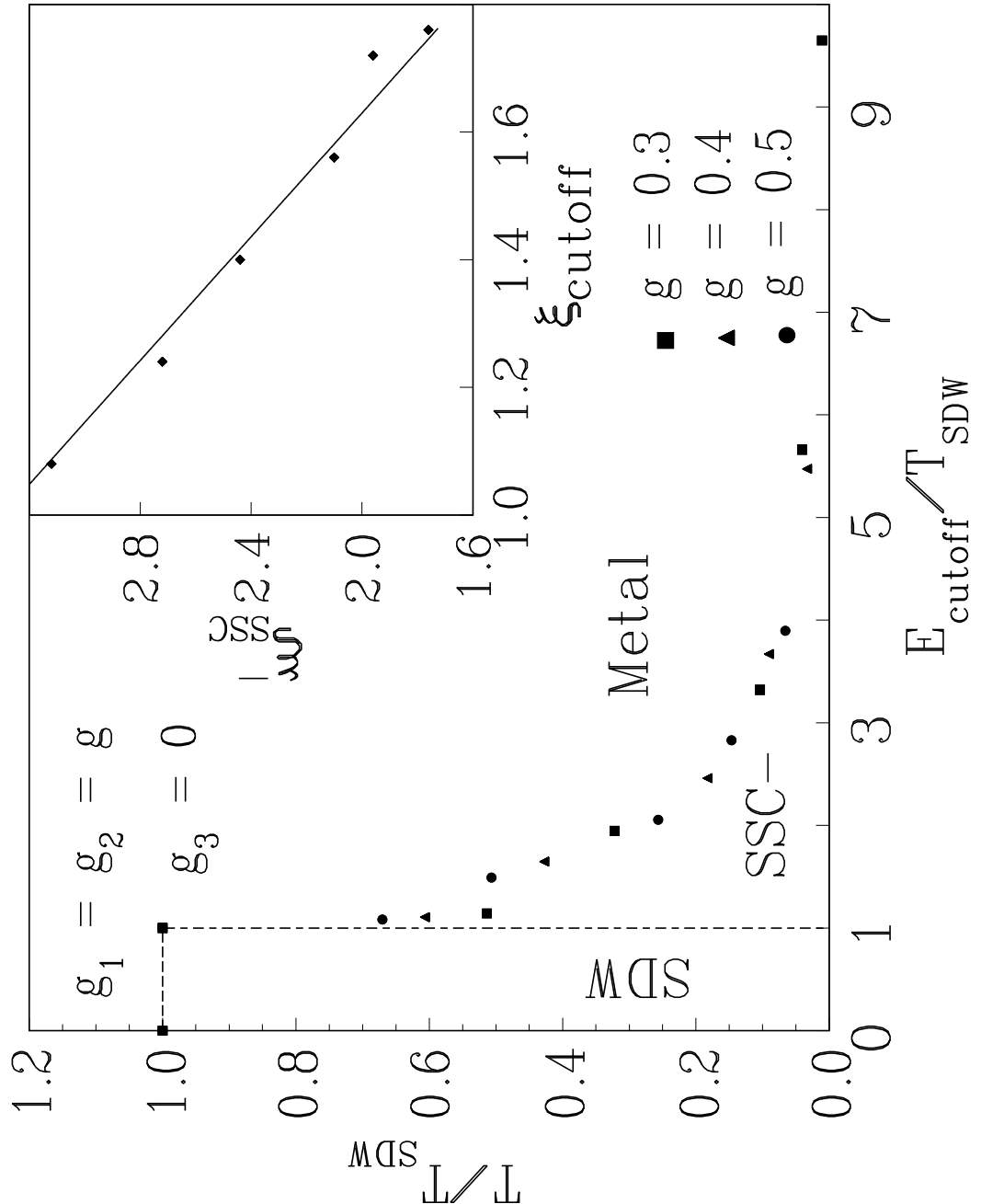


FIG. 17. Phase diagram of the Hubbard model without umklapp illustrates the dependence of the d -wave superconducting transition temperature T_{SSC}^- on the cutoff energy E_{cutoff} for different g . The inset shows the same dependence in the logarithmic variables ξ_{SSC}^- and ξ_{cutoff} . The solid line in the inset is a fit: $\xi_{SSC}^- = a - b \xi_{cutoff}$, $a = 5.33$, $b = 2.06$.

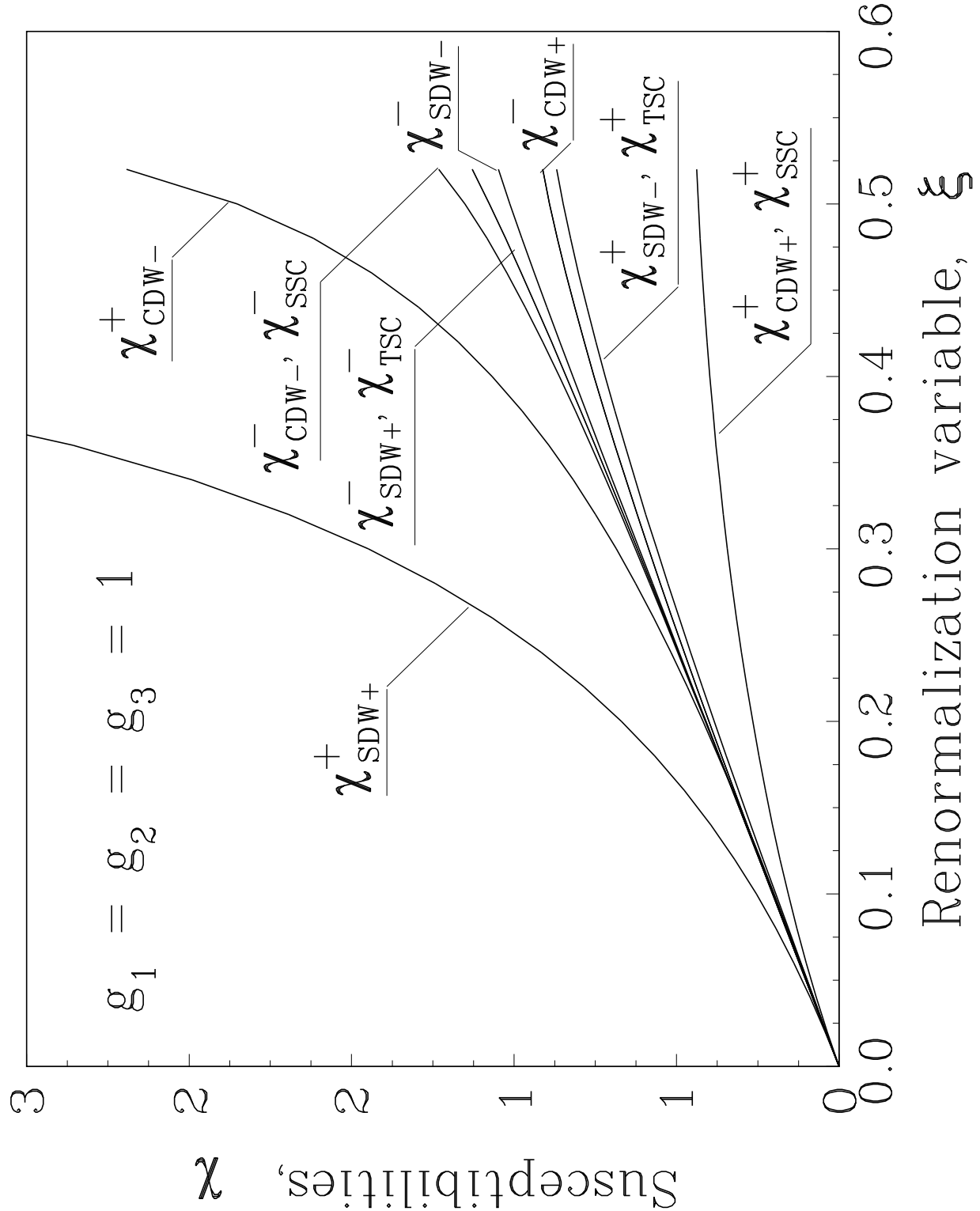


FIG. 18. Evolution of generalized susceptibilities $\chi_i(\xi)$ in the Hubbard model with umklapp scattering. $\chi_{\text{SDW}+}^+(\xi)$ diverges at $\xi = \xi_{\text{SDW}+}^+ = 0.54$.

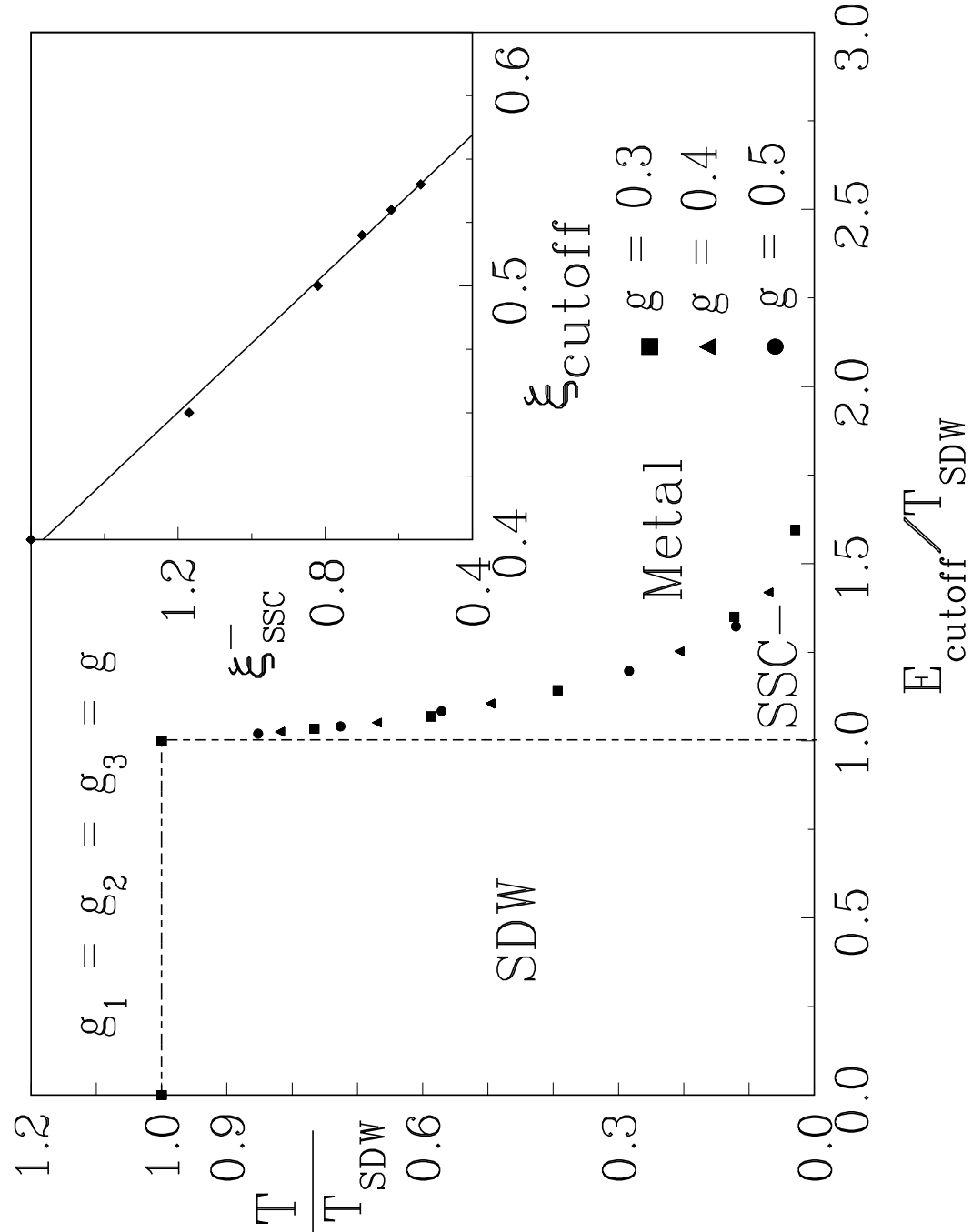


FIG. 19. Phase diagram of the Hubbard model with umklapp scattering illustrates the dependence of the critical temperature T_{SSC}^- on the cutoff energy E_{cutoff} for different g . The inset shows the dependence of ξ_{SSC}^- on ξ_{cutoff} . The solid line in the inset is a fit: $\xi_{SSC}^- = a - b \xi_{cutoff}$, $a = 4.5$, $b = 7.32$.

